

# Abundances of disk and bulge giants from high-resolution optical spectra

## III. Sc, V, Cr, Mn, Co, Ni<sup>★,★★</sup>

M. Lomaeva<sup>1</sup>, H. Jönsson<sup>1</sup>, N. Ryde<sup>1</sup>, M. Schultheis<sup>2</sup>, and B. Thorsbro<sup>1</sup>

<sup>1</sup> Lund Observatory, Department of Astronomy and Theoretical Physics, Lund University, Box 43, 221 00 Lund, Sweden  
e-mail: nat13ml@student.lu.se

<sup>2</sup> Observatoire de la Côte d'Azur, Boulevard de l'Observatoire, B.P. 4229, 06304 Nice Cedex 4, France

Received 14 September 2018 / Accepted 25 February 2019

### ABSTRACT

**Context.** The formation and evolution of the Galactic bulge and the Milky Way is still a debated subject. Observations of the X-shaped bulge, cylindrical stellar motions, and the presumed existence of a fraction of young stars in the bulge have suggested that it formed through secular evolution of the disk and not through gas dissipation and/or mergers, as thought previously.

**Aims.** Our goal was to measure the abundances of six iron-peak elements (Sc, V, Cr, Mn, Co, and Ni) in the local thin and thick disks and in the bulge. These abundances can provide additional observational constraints for Galaxy formation and chemical evolution models, and help us to understand whether the bulge has emerged from the thick disk or not.

**Methods.** We use high-resolution optical spectra of 291 K giants in the local disk mostly obtained by the FIES at NOT (signal-to-noise ratio (S/N) of 80–100) and 45 K giants in the bulge obtained by the UVES/FLAMES at VLT (S/N of 10–80). The abundances are measured using Spectroscopy Made Easy (SME). Additionally, we apply non-local thermodynamic equilibrium corrections to the ratios [Mn/Fe] and [Co/Fe]. The thin and thick disks were separated according to their metallicity, [Ti/Fe], as well as proper motions and the radial velocities from *Gaia* DR2.

**Results.** The trend of [V/Fe] vs. [Fe/H] shows a separation between the disk components, being more enhanced in the thick disk. Similarly, the [Co/Fe] vs. [Fe/H] trend shows a hint of an enhancement in the local thick disk. The trends of V and Co in the bulge appear to be even more enhanced, although within the uncertainties. The decreasing value of [Sc/Fe] with increasing metallicity is observed in all the components, while our [Mn/Fe] value steadily increases with increasing metallicity in the local disk and the bulge instead. For Cr and Ni we find a flat trend following iron for the whole metallicity range in the disk and the bulge. The ratio of [Ni/Fe] appears slightly overabundant in the thick disk and the bulge compared to the thin disk, although the difference is minor.

**Conclusions.** The somewhat enhanced ratios of [V/Fe] and [Co/Fe] observed in the bulge suggest that the local thick disk and the bulge might have experienced different chemical enrichment and evolutionary paths. However, we are unable to predict the exact evolutionary path of the bulge solely based on these observations. Galactic chemical evolution models could, on the other hand, allow us to predict them using these results.

**Key words.** Galaxy: evolution – solar neighborhood – stars: abundances

## 1. Introduction

One of the most important questions in contemporary astrophysics concerns the formation and evolution of galaxies (Bland-Hawthorn & Gerhard 2016). The Milky Way is a typical barred spiral galaxy and is the only such galaxy where we can resolve individual stars for a detailed analysis. To fully understand the formation of the Milky Way, it is essential to understand the formation of its central region, the bulge. The view on the origin of the bulge has changed drastically over the past years. Previously, the bulge was thought to belong to the

group of spherically shaped classical bulges formed through dissipation of gas (e.g. Eggen et al. 1962; Chiappini et al. 1997; Micali et al. 2013) or merging events according to the  $\Lambda$  cold dark matter ( $\Lambda$ CDM) theory (e.g. Abadi et al. 2003; Scannapieco & Tissera 2003). However, this view has been challenged by new observations revealing properties of the Milky Way bulge that are not typical for classical bulges.

These new observations include kinematic observations from the Apache Point Observatory Galactic Evolution Experiment (APOGEE; Zasowski et al. 2016; Ness et al. 2016); the X-shape of the bulge, which represents the inner 3D part of the Galactic bar (McWilliam & Zoccali 2010; Nataf et al. 2010; Wegg & Gerhard 2013); cylindrical rotation of the bulge stars from the BRAVA (Kunder et al. 2012) and ARGOS (Ness et al. 2013) surveys; and a population of presumably young stars found in the bulge. van Loon et al. (2003) found stars as young as  $\lesssim 200$  Myr across the inner bulge. More recent studies of blue stragglers by Clarkson et al. (2011) and microlensed dwarfs by Bensby et al. (2017) have suggested that there is a fractional stellar component

\* Full Tables A.1–A.5 are only available at the CDS via anonymous ftp to [cdsarc.u-strasbg.fr](https://cdsarc.u-strasbg.fr) (130.79.128.5) or via <http://cdsarc.u-strasbg.fr/viz-bin/qcat?J/A+A/625/A141>

\*\* Based on observations made with the Nordic Optical Telescope (programs 51-018 and 53-002), operated by the Nordic Optical Telescope Scientific Association at the Observatorio del Roque de los Muchachos, La Palma, Spain, of the Instituto de Astrofísica de Canarias, and using spectral data retrieved from PolarBase at Observatoire Midi Pyrénées.

in the bulge with ages  $\lesssim 5$  Gyr. A generation with ages  $\lesssim 5$  Gyr was also discovered by [Bernard et al. \(2018\)](#) who studied deep color-magnitude diagrams of four bulge fields.

The new discoveries point towards the bulge being dynamically formed and having the boxy/peanut (b/p) shape that has also been observed in many other spiral galaxies ([Lütticke et al. 2000](#); [Kormendy & Kennicutt 2004](#)). Several N-body simulations of the evolution of spiral galaxies have managed to reproduce the b/p bulge shape through secular disk instabilities (e.g. [Combes & Sanders 1981](#); [Athanassoula 2005](#); [Martinez-Valpuesta et al. 2006](#)). In these simulations, stellar bars experience one or even multiple buckling instabilities that can result in a boxy or peanut-shaped structure depending on the viewing angle (e.g. [Di Matteo et al. 2014](#); [Fragkoudi et al. 2018](#)). Moreover, bulges formed through disk instabilities, being of disk origin ([Fragkoudi et al. 2018](#)), can and actually might be expected to contain young stars ([Gonzalez & Gadotti 2016](#)).

However, the structure of the bulge does not appear to be homogeneous. Different kinematic properties measured by APOGEE of populations of different metallicities ([Zasowski et al. 2016](#)) provide evidence for different evolutionary histories of these populations, and the metallicity distribution maps found by the GIBS survey ([Zoccali et al. 2017](#)) and APOGEE ([García Pérez et al. 2018](#)) show the presence of different populations. [Babusiaux et al. \(2010\)](#) studied kinematics (radial velocities and proper motions) and metallicities of a sample of bulge stars spread out over different latitudes and concluded that metal-rich stars can be associated with a barred population, while the metal-poor stars can be associated with a spheroidal component or potentially the inner thick disc. Additionally, [Ness et al. \(2013\)](#) and [Vásquez et al. \(2013\)](#), who also studied the chemo-dynamical properties of bulge stars, arrived at the conclusion that the metal-rich stars in their sample belong to the X-shaped bulge, whereas the metal-poor stars do not. These results and some dynamical simulations (e.g. [Di Matteo et al. 2014](#)) allow the existence of a minor spherical component, while most of the mass in the bulge originates from the disk. [Shen et al. \(2010\)](#) modeled the cylindrical rotation in the bulge and concluded that the maximum mass of the spheroidal component can be 8% of the disk mass in order to reproduce the BRAVA observations. Evidently, the formation of the Galaxy and the bulge is a complex matter and is still not fully understood as no successful fully self-consistent models for the bulge in the cosmological framework are available today ([Barbuy et al. 2018](#)).

In order to observationally constrain potential formation routes, abundance ratios can be measured to constrain the star formation rate (SFR) and initial mass function (IMF) of a population, for example. To quantify the SFR and IMF in the bulge,  $[\alpha/\text{Fe}]$  versus  $[\text{Fe}/\text{H}]$  trends have been used extensively ([Matteucci 2012](#)). [Bensby et al. \(2010\)](#), among others, studied  $\alpha$ -trends of K giant stars in the bulge and inner thick disk (galactocentric radius of 4–7 kpc) and found chemical similarities, also between the inner and local thick disks. Later, [Bensby et al. \(2017\)](#) compared their  $\alpha$ -trends of dwarf stars in the local thick disk and bulge and found that there is no significant variation in IMF; however, the  $[\alpha/\text{Fe}]$  “knee” appears at slightly higher metallicities in the bulge than in the local thick disk. They note that this question should be further investigated by analyzing larger stellar samples.

In the first two papers in this series, [Jönsson et al. \(2017a,b\)](#) worked on the same spectra of disk and bulge giants as we use in this paper, and determined their  $\alpha$ -abundances, which led to the conclusion that the bulge generally follows the thick disk trend, again indicating similar chemical evolution histories.

These results could probably indicate a slightly higher SFR in the bulge as well since the bulge trends of Mg, Ca, and Ti trace the upper envelope of the thick disk trends.

[Johnson et al. \(2014\)](#) examined  $\alpha$ - and iron-peak abundances in bulge giants and arrived at a different result: while no special IMF is required to reproduce the bulge trends, they conclude that the bulge and the thick disk have experienced different chemical enrichment paths. This conclusion was drawn from the enhanced abundance trends, in particular of the iron-peak elements such as Co, Ni, and Cu, in the bulge compared to the thick disk. In the analysis, however, their reference sample consisted of disk dwarfs, and this sort of comparison using dwarfs and giants is likely to be affected by potential systematic offsets (see [Meléndez et al. 2008](#); [Alves-Brito et al. 2010](#)).

[Bensby et al. \(2017\)](#), however, did not find such an enhancement for Ni in the bulge. The trend of a different iron-peak element, Mn, has also been a subject of disagreement in terms of the separation between the thin and thick disk components ([Feltzing et al. 2007](#); [Battistini & Bensby 2015](#)).

From the APOGEE survey there have been two papers discussing abundance trends in the bulge: [Schultheis et al. \(2017\)](#) and [Zasowski et al. \(2019\)](#). Regarding iron-peak elements, they both investigate Cr, Mn, Co, and Ni, and [Zasowski et al. \(2019\)](#) compare similarly analyzed stars in the local disk. For Cr, and possibly Co, they find differences in the local and bulge trends, while the trends for Mn and Ni seem very similar in the two populations.

Clearly, the literature studies have not arrived at a common conclusion, as some are finding similarities and others find differences between the evolutionary paths of the disk and the bulge. A manual, homogeneous spectroscopic analysis of the same type of stars in these Galactic components, examining other elements than the extensively studied  $\alpha$ -elements, can give new insights into the question of whether the bulge emerged from the disk.

Iron-peak elements, as mentioned above, are suitable for such Galactic archaeology studies, being able to probe the chemical enrichment history. In this paper, we examine iron-peak elements with atomic numbers  $21 \leq Z \leq 28$ , i.e. Sc, V, Cr, Mn, Fe, Co, and Ni<sup>1</sup>. Great progress has been made in understanding their nucleosynthetic sites and production, but it is still a subject for debate. Especially for Sc, V, and Co, the observational trends cannot be reproduced with galactic chemical evolution models, and for Mn the uncertainties in the observed trends need further investigation; however, for Cr and Ni the situation is better.

Iron-peak elements are synthesized in thermonuclear and in core-collapse supernovae (SNe). As for  $\alpha$ -elements, SNe II are presumed to be the main source of Sc ([Clayton 2003](#), hereafter C03). Whereas V is thought to be mostly created in SNe Ia (C03), Cr is created in SNe Ia and SNe II in comparable amounts (C03). This is also true for the heavier iron-peak elements, Fe, Co, and Ni, even though they are formed through other nucleosynthetic channels (C03). The understanding of the synthesis of Mn is more complicated with possible sites in both SNe Ia and SNe II. For SNe Ia, the amount of Mn yields depend on the properties of the progenitor white dwarf (e.g. [Nomoto et al. 1997](#); [Yamaguchi et al. 2015](#)).

In this work, we continue the study begun in [Jönsson et al. \(2017a,b\)](#) where abundances of O, Mg, Ca, and Ti were determined; examine the iron-peak elements Sc, V, Cr, Mn, Co, and

<sup>1</sup> Titanium is often defined as an  $\alpha$ -element, but sometimes also as an iron-peak element (e.g. [Snedden et al. 2016](#)).

Ni; and conduct a homogeneous giant–giant comparison of the local disks and the bulge.

## 2. Observations

### 2.1. Solar neighborhood sample

In the solar neighborhood sample there are 291 K giants. Most of these stars were observed under program 51-018 (150 stars) in May–June 2015 and under program 53-002 (63 stars) in June 2016 using the FIBre-fed Echelle Spectrograph (FIES; [Telting et al. 2014](#)) installed on the Nordic Optical Telescope (NOT). Forty-one spectra were taken from [Thygesen et al. \(2012\)](#) in turn from FIES/NOT, 18 were downloaded from the FIES archive, and 19 spectra were taken from the NARVAL<sup>2</sup> and ESPaDOnS<sup>3</sup> spectral archive in the PolarBase data base ([Petit et al. 2014](#)).

The resolving power of the FIES spectra is  $R \sim 67\,000$  and for PolarBase it is  $R \sim 65\,000$ . The entire optical spectrum was covered by these instruments, but the wavelength region was restricted to 5800–6800 Å in order to match the wavelength region of the bulge spectra, providing a more homogeneous analysis.

The majority of the observed stars are quite bright, see Table A.1, and the corresponding observing time is in many cases on the order of minutes. For the 213 FIES stars, the “exp-count” feature was used during the observations which allows the exposure to be aborted when a certain CCD count level has been obtained. The signal-to-noise ratios (S/N) of the FIES spectra are generally high, between 80 and 120 per data point in the reduced spectrum, see Table A.1; roughly the same applies to the spectra from PolarBase. Spectra from [Thygesen et al. \(2012\)](#) have a lower S/N of about 30–50. The S/N values were measured by the IDL-routine `der_snr.pro`<sup>4</sup> and are listed in Table A.1.

The reduction of the FIES spectra was preformed using the standard FIES pipeline. The spectra from [Thygesen et al. \(2012\)](#) and PolarBase were already reduced and ready to use. An initial, rough normalization of all spectra was done with the IRAF task `continuum`. However, in the analysis, the continuum is normalized more carefully by fitting a straight line to continuum regions in every short wavelength window examined. No removal of atmospheric telluric lines or subtraction of the sky emission lines was attempted; they were avoided by making a comparison to the radial velocity shifted telluric spectrum of the Arcturus atlas of [Hinkle et al. \(2000\)](#).

Most of the stars from the thick disk lie at a distance of ~45–2000 pc from the Sun, whereas the majority of the thin disk stars are located ~30–1000 pc away (estimations from [McMillan 2018](#)). The separation of the disk components is discussed in Sect. 3.5.

### 2.2. Galactic bulge sample

The Galactic bulge sample consists of 45 K giants, see Table A.2. The spectra were obtained using the spectrometer FLAMES/UVES installed at the VLT. In total, with the original aim of attempting to investigate gradients, five fields were observed: SW, BW, BL, B3, and B6. The naming convention of these fields is based on that of [Lecureur et al. \(2007\)](#): B3 means a field at  $b = -3^\circ$ , B6 a field at  $b = -6^\circ$  along the Galactic minor axis; SW and BW refers to the Sagittarius Window and Baade’s

Window, respectively; and BL to the Blanco field. The definition of the extent of the bulge is a bit blurred (see discussion in [Barbuy et al. 2018](#)), but with the [Barbuy et al. \(2018\)](#) definition of the bulge being the region on the sky within  $b = \pm 10^\circ$  and  $l = \pm 10^\circ$ , the Blanco field is on the verge of being a bulge field; nevertheless, we include it in our bulge compilation to be consistent with [Lecureur et al. \(2007\)](#) and [Johnson et al. \(2014\)](#), among others. The fields are indicated in Fig. 1 together with the outline of the Galactic bulge ([Weiland et al. 1994](#)); the positions of the microlensed dwarfs from [Bensby et al. \(2017\)](#); and the fields analyzed in [Barbuy et al. \(2013\)](#), [Ernandes et al. \(2018\)](#), [Johnson et al. \(2014\)](#), and [Schultheis et al. \(2017\)](#), studies that we discuss in Sect. 5.2.2. Due to the dust extinction it is difficult to observe bulge stars in the optical wavelength range, and for this reason it was only possible to observe stars in the outer part of the bulge. Observations of stars in the immediate center require observations in the IR. However, determining the stellar parameters for these observations is still difficult (e.g. [Rich et al. 2012](#)), but progress is being made (e.g. [Ryde et al. 2016](#); [Schultheis et al. 2016](#); [Rich et al. 2017](#); [Nandakumar et al. 2018](#)).

The 34 stars in the fields B3, BW, B6, and BL were observed in May–August 2003–2004, while the 11 stars in the SW field were observed in August 2011 (ESO program 085.B-0552(A)). With FLAMES/UVES it is possible to observe seven stars in each pointing. Depending on the extinction, each setting requires an integration time of 5–12 h. The achieved S/N of the spectra in this sample are significantly lower than those for the stars in the solar neighborhood sample, ranging between 10 and 80. The resolving power of the bulge spectra is  $R \approx 47\,000$  and the wavelength coverage is between 5800 and 6800 Å.

All of the stars in the bulge sample apart from one have a parallax uncertainty above 20% as measured by *Gaia* DR2 ([Gaia Collaboration 2016, 2018](#)) resulting in rather uncertain distance estimations. Nevertheless, [Bailer-Jones et al. \(2018\)](#) estimate that most of these stars lie 4–12 kpc away, with a tendency to lower values. This means that our stars are spread out over the area occupied by the bulge/bar ([Wegg et al. 2015](#)). We expect higher reliability of distances for our bulge stars from coming *Gaia* data releases.

## 3. Analysis

The analysis in this investigation is performed in the same manner as in first papers of this series ([Jönsson et al. 2017a,b](#)). In general, every observed spectral line of interest is fitted, by means of a  $\chi^2$  minimization, with synthetic spectra modeling the line strengths and profiles for a given set of stellar parameters, as determined in [Jönsson et al. \(2017a,b\)](#). The atomic line data needed is described in Sect. 3.1 and the spectral synthesizing tool, Spectroscopy Made Easy (SME), in Sect. 3.2. The model atmospheres that are used and interpolated for in SME are described in Sect. 3.3. We also discuss the previously determined photospheric stellar parameters for our stars in Sect. 3.4. The method used for discriminating between the thin and thick disk is described in Sect. 3.5.

### 3.1. Line data

The line data used in the determination of chemical abundances for all elements apart from Sc were taken from the *Gaia*-ESO line list version 5 ([Heiter et al. 2015](#), and in prep.). For odd-Z elements<sup>5</sup>, we have to consider the hyperfine splitting (hfs) of

<sup>2</sup> Mounted on Telescope *Bernard Lyot* (TBL).

<sup>3</sup> Mounted on the Canada–France–Hawaii Telescope (CFHT).

<sup>4</sup> See [stecf.org/software/ASTROsoft/DER\\_SNR](http://stecf.org/software/ASTROsoft/DER_SNR)

<sup>5</sup> Here: Sc, V, Co, and Mn.

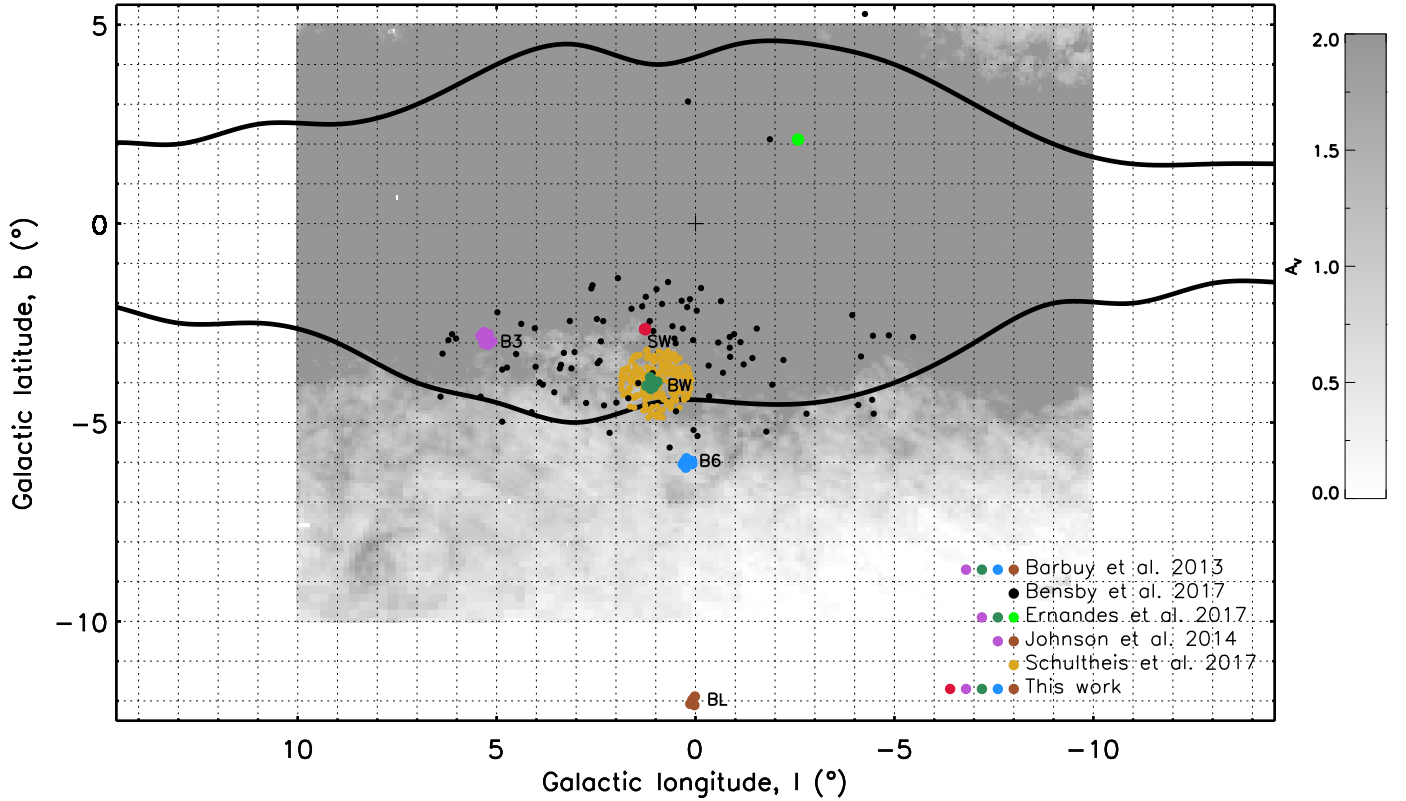


**Fig. 1.** Map of the Galactic bulge showing the five analyzed fields (SW, B3, BW, B6, and BL). The positions of the microlensed dwarfs from Bensby et al. (2017) and the fields analyzed in Barbuy et al. (2013), Ernandes et al. (2018), Johnson et al. (2014), and Schultheis et al. (2017) are also marked in the figure. The dust extinction towards the bulge is taken from Gonzalez et al. (2011, 2012) scaled to optical extinction (Cardelli et al. 1989). The scale saturates at  $A_V = 2$ . The COBE/DIRBE contours of the Galactic bulge are from Weiland et al. (1994).

atomic energy levels, that will have a desaturating effect on strong atomic lines (Prochaska & McWilliam 2000; Thorsbro et al. 2018). Since the hfs components for Sc were not present in the *Gaia*-ESO line list, they were instead taken from the updated version of the VALD line list (Kupka et al. 1999; Pakhomov et al. 2017), see Table A.3. All lines used, apart from those of Sc, are from the neutral species. The Sc lines are from Sc II.

We took several precautions to try to avoid blended lines: first we followed the recommendations from *Gaia*-ESO (Heiter et al. 2015), then we carefully scanned our selected lines for visible blends in all stars, and finally we determined abundances for all lines individually to make sure they reproduce the same abundance trends with metallicity.

### 3.2. Spectral line synthesis

For abundance measurements, we used the spectral line synthesizer Spectroscopy Made Easy (SME; Valenti & Piskunov 1996; Piskunov & Valenti 2017). SME can simultaneously fit global stellar photospheric parameters and/or – as done in this work – abundances based on user defined line masks covering spectral lines of interest. To this end, synthetic model spectra of different abundances are synthesized on the fly, and the best fit of the line profile to the observed data is found utilising the  $\chi^2$  minimization method as described in Marquardt (1963). For the elements with several lines of suitable strength available (see Table A.3), all lines were fitted simultaneously, but investigatory individual fits were also performed to make sure that no line was systematically deviating from the others. The other abundances in the calculation of the synthetic spectra are solar, by default from

Grevesse et al. (2007), scaled with metallicity unless defined otherwise, which we do for the  $\alpha$  elements, determined in Jönsson et al. (2017b).

### 3.3. Model atmospheres

We used the grid of local thermodynamic equilibrium (LTE) MARCS models (Gustafsson et al. 2008) supplied with SME, which consists of a subsample of the models available on the MARCS webpage<sup>6</sup>. The model grid is  $\alpha$ -enhanced according to the standard MARCS scheme with  $[\alpha/\text{Fe}] = +0.4$  for  $[\text{Fe}/\text{H}] < -1$ ,  $[\alpha/\text{Fe}] = 0.0$  for  $[\text{Fe}/\text{H}] > 0$ , and linearly falling in between, while the other abundances are solar values simply scaled with metallicity. The models are spherically symmetric for  $\log g < 3$ , and plane parallel otherwise. For the spectral synthesis, SME interpolates in this grid of model atmospheres, keeping the unfitted abundances consistent with the grid of model atmospheres. While this on-the-fly spectral synthesis is made under the assumption of LTE, we later add available non-LTE (NLTE) abundance corrections for the Co and Mn trends.

### 3.4. Photospheric stellar parameters

All photospheric stellar parameters used here were determined in Jönsson et al. (2017a,b). Briefly, they were estimated by simultaneously fitting a synthetic spectrum using the same version of SME and model atmosphere grid for unsaturated and unblended Fe I, Fe II, and Ca I lines, as well as  $\log g$  sensitive Ca I wings,

<sup>6</sup> See [marcs.astro.uu.se](http://marcs.astro.uu.se)

while  $T_{\text{eff}}$ ,  $\log g$ ,  $[\text{Fe}/\text{H}]$ ,  $v_{\text{mic}}$ , and  $[\text{Ca}/\text{Fe}]$  were set as free parameters. NLTE corrections for Fe I from Lind et al. (2012) were accounted for when calculating the atmospheric parameters, but these were very small. For more details see Jönsson et al. (2017a,b).

Representative uncertainties in the stellar parameters for a disk star of  $S/N \sim 100$  (per data point in the reduced spectrum as measured by `der_snr.pro`) are  $\pm 50$  K for  $T_{\text{eff}}$ ,  $\pm 0.15$  dex for  $\log g$ ,  $\pm 0.05$  dex for  $[\text{Fe}/\text{H}]$ , and  $\pm 0.1$  km s $^{-1}$  for  $v_{\text{mic}}$ , but their magnitudes of course depend on the  $S/N$  (see Fig. 2 in Jönsson et al. 2017a).

### 3.5. Thin and thick disk separation

The thin and thick disk stellar populations show some substantial differences in  $[\alpha/\text{Fe}]$ , kinematics, and ages.

Ages of giant stars are rather hard to determine due to the strong overlap of isochrones on the red giant branch (RGB). The Galactic space velocities ( $U, V, W$ ) can be used as well; however, Bensby et al. (2014) found that stellar ages of dwarfs act as a better discriminator between the thick and thin disk than the kinematics, although they note that stellar ages are often subjected to larger uncertainties. They also saw an age- $[\alpha/\text{Fe}]$  relation by studying the ratio  $[\text{Ti}/\text{Fe}]$  as it shows a clear enhancement of the thick disk. They concluded that dwarf and subgiant stars older than 8 Gyr exhibit higher  $[\text{Ti}/\text{Fe}]$  values, and Ti abundances can therefore be used to distinguish between the old and young stellar populations, at least in the solar neighborhood.

For this reason, and also given the clear separation between the disk components in the  $[\text{Ti}/\text{Fe}]$  versus  $[\text{Fe}/\text{H}]$  trend for giant stars (Jönsson et al. 2017a), we use the  $[\text{Fe}/\text{H}]$  and  $[\text{Ti}/\text{Fe}]$  abundances measured in that paper as well as the proper motions and radial velocities from Table A.1 and *Gaia* DR2 (Gaia Collaboration 2016, 2018) to calculate the total space velocity,  $V_{\text{tot}}$ <sup>7</sup>, to assign the stars to either the thin or thick disks. For thick disk stars,  $V_{\text{tot}}$  is generally higher than for the thin disk (Nissen 2004). The kinematic data were available for 268 stars in our sample, and to convert those into ( $U, V, W$ ) velocity components we used tools from the *astropy* package, and *Gaia* DR2 distance estimates from McMillan (2018). The remaining stars without kinematics were not considered in the separation; however, they are used in the following cases where the disk sample is considered as a whole.

The separation itself was done using a clustering method called Gaussian Mixture Model (GMM), which was obtained from the *scikit-learn* module written in Python (Pedregosa et al. 2011), which contains the *GaussianMixture* package. The GMM is a parametric probability density function (pdf) which is represented as a weighted sum of Gaussian component densities, i.e. the overall distribution of the data points is assumed to consist of one- or multi-dimensional Gaussian subdistributions. The parameters of the complete GMM (mean vectors, covariance matrices, and mixture weights from all component densities) can be estimated from training data utilising the iterative expectation-maximisation (EM) algorithm. Broadly speaking, the EM algorithm first calculates the probability that the data points belong to one of the clusters, and then updates the parameters of the Gaussian subdistributions using the estimated membership probabilities. Each iteration of the EM algorithm increases the log-likelihood of the model improving the fit to the data until it converges. However, the number of clusters has to be known in advance. Here the number of clusters was set to

<sup>7</sup>  $V_{\text{tot}}^2 \equiv U^2 + V^2 + W^2$ .

two. For a thorough mathematical description, see, e.g. Reynolds (2009).

To check the validity of the clustering, we applied the separation of the disk stars onto the trends of the  $\alpha$ -elements in Jönsson et al. (2017a), as shown in Fig. 2. This separation was then applied to the iron-peak abundance trends. We note that in the separation no  $S/N$  cut was performed and abundance uncertainties were not considered.

## 4. Results

The determined abundances and the obtained abundance trends of the iron-peak elements studied in the disk and the bulge are listed in Tables A.4 and A.5 and are shown in Figs. 3 and 4. To highlight the features of the trends, also shown are the plots of the running mean and running  $1\sigma$  scatter. The number of data points in the running window was set to 29 for the thin and thick disk samples, and 14 for the bulge. Therefore, the running mean and  $1\sigma$  scatter does not cover the whole trend range. The running median was tested as well, but the results were very similar so all conclusions and discussion would be qualitatively the same.

### 4.1. Solar neighborhood

The solar neighborhood stellar sample consists of 291 K giants, where 268 had available kinematic data, of which 71 likely belong to the thick disk population and 197 to the thin disk. A rather clear separation between the disk components is seen in the trend of V; for Co, there is a minor overlap; and a larger overlap is seen for Sc and Ni. For the Cr and Mn disk trends, the overlap is very prominent.

The thick disk trend of Sc in Fig. 3 is somewhat enhanced at the low-metallicity end reaching  $[\text{Sc}/\text{Fe}] \sim +0.25$  dex (hereafter we refer to the running mean when describing  $[\text{X}/\text{Fe}]$ ). As  $[\text{Fe}/\text{H}]$  increases,  $[\text{Sc}/\text{Fe}]$  goes down to  $\sim +0.1$  dex. The average  $\langle [\text{Sc}/\text{Fe}] \rangle$  value of the thick disk is  $+0.17$  dex with a mean scatter,  $\langle \sigma \rangle$ , of 0.05 dex. The thin disk trend has the highest  $[\text{Sc}/\text{Fe}]$  value of  $\sim +0.15$  dex at  $[\text{Fe}/\text{H}] \sim -0.4$  which decreases to  $\sim 0$  and flattens out at  $[\text{Fe}/\text{H}] \sim -0.2$ . This plateau remains even at supersolar metallicities. The average elevation of the  $\langle [\text{Sc}/\text{Fe}] \rangle$  value in the thin disk is  $+0.03$  dex with  $\langle \sigma \rangle = 0.04$  dex. In the region where the thin and thick disk overlaps, the thick disk trend is enhanced compared to the thin disk, but the uncertainties of the trends highly overlap.

The  $[\text{V}/\text{Fe}]$  versus  $[\text{Fe}/\text{H}]$  trend shows an enhancement of  $\sim +0.15$  dex in the thick disk trend at  $[\text{Fe}/\text{H}] \lesssim -0.4$ . The trend gradually decreases with increasing metallicity reaching  $[\text{V}/\text{Fe}] \sim +0.1$  dex at  $[\text{Fe}/\text{H}] \sim -0.1$ . The mean  $\langle [\text{V}/\text{Fe}] \rangle$  value of the thick disk is  $+0.14$  dex and  $\langle \sigma \rangle = 0.04$  dex. The thin disk  $[\text{V}/\text{Fe}]$  value is relatively constant and nearly zero, apart from a slight increase at supersolar metallicities. The average thin disk  $\langle [\text{V}/\text{Fe}] \rangle$  value is  $\sim 0$  dex and  $\langle \sigma \rangle = 0.05$  dex.

The ratios of  $[\text{Cr}/\text{Fe}]$  in the disk components exhibit flat trends throughout the whole metallicity range apart from slight enhancements at the highest metallicities in each Galactic component. The mean  $\langle [\text{Cr}/\text{Fe}] \rangle$  value is  $\sim 0$  dex with average  $\langle \sigma \rangle \sim 0.04$  dex for the thin and thick disks.

The lowest  $[\text{Mn}/\text{Fe}]$  value is observed in the thick disk trend with the running mean reaching down to  $\sim -0.3$  dex at  $[\text{Fe}/\text{H}] \sim -0.6$ . The trend steadily increases with increasing metallicity and attains  $[\text{Mn}/\text{Fe}] \sim -0.1$  dex at  $[\text{Fe}/\text{H}] \sim -0.1$ . The mean  $\langle [\text{Mn}/\text{Fe}] \rangle$  value in the thick disk is  $\sim -0.2$  dex and  $\langle \sigma \rangle = 0.08$  dex. The lowest  $[\text{Mn}/\text{Fe}]$  value of the thin disk is  $\sim -0.2$  dex at  $[\text{Fe}/\text{H}] \sim -0.4$ . The trend also increases steadily

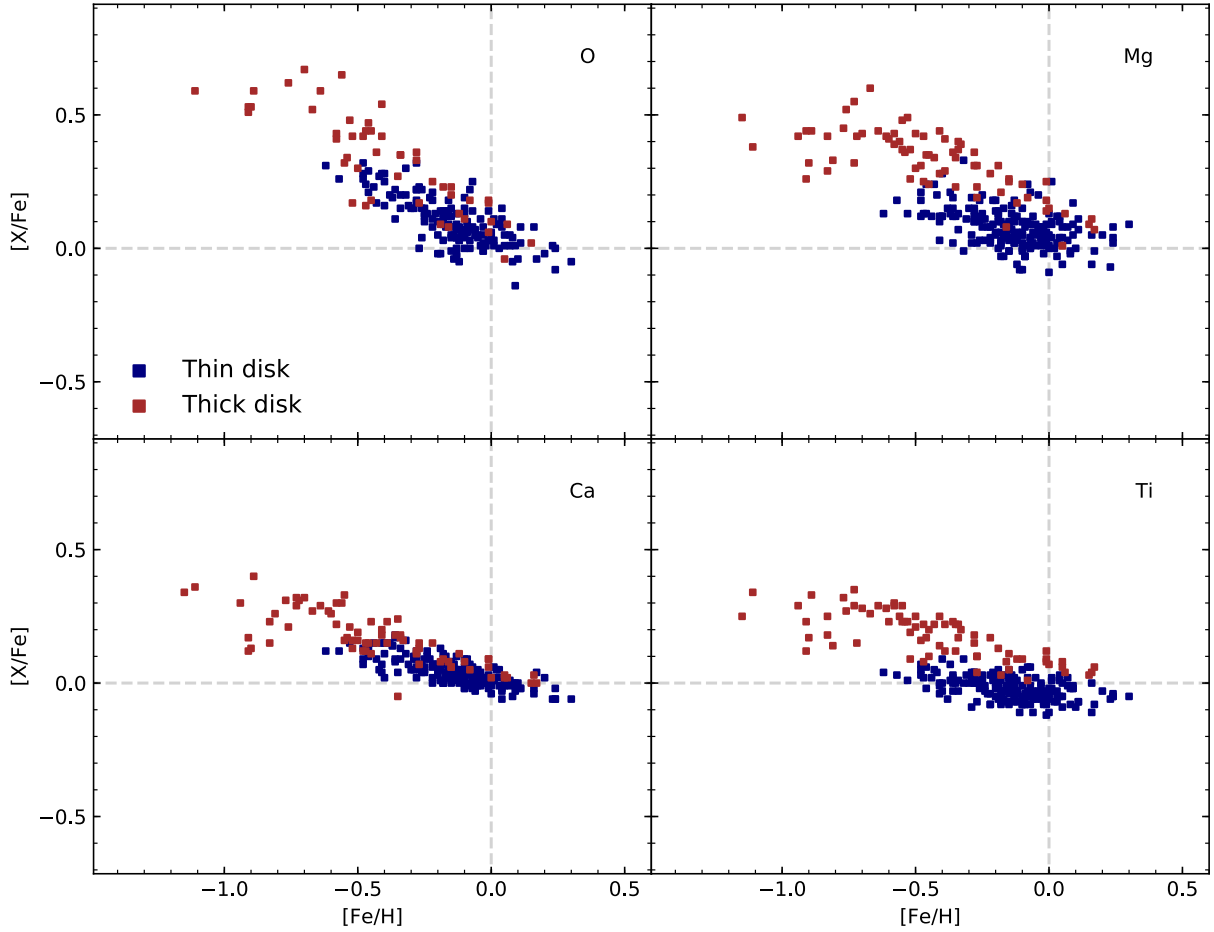


**Fig. 2.** Thin and thick disk separation (blue and red squares, respectively) applied on the  $[(\text{O, Mg, Ca, Ti})/\text{Fe}]$  vs.  $[\text{Fe}/\text{H}]$  trends from Jönsson et al. (2017a). The plots are shown in the same manner as in Jönsson et al. (2017a), i.e. with the solar abundances from Asplund et al. (2009).

to  $[\text{Mn}/\text{Fe}] \sim -0.02$  dex at  $[\text{Fe}/\text{H}] \sim +0.1$ . The average  $\langle [\text{Mn}/\text{Fe}] \rangle$  value in the thin disk is  $-0.14$  dex with  $\langle \sigma \rangle = 0.06$  dex.

The thick disk trend of cobalt gradually decreases from  $[\text{Co}/\text{Fe}] \sim +0.2$  dex at  $[\text{Fe}/\text{H}] \sim -0.7$  to  $[\text{Co}/\text{Fe}] \sim +0.1$  dex at  $[\text{Fe}/\text{H}] \sim -0.1$ . The thin disk trend goes down from  $[\text{Co}/\text{Fe}] \sim +0.1$  dex at  $[\text{Fe}/\text{H}] \sim -0.4$  to  $[\text{Co}/\text{Fe}] \sim +0.05$  dex at  $[\text{Fe}/\text{H}] \sim -0.1$ . At  $[\text{Fe}/\text{H}] \gtrsim -0.1$ , the thin disk trend starts to increase to  $[\text{Co}/\text{Fe}] \sim +0.1$  dex at supersolar metallicities. The average  $\langle [\text{Co}/\text{Fe}] \rangle$  for our thick disk trend is  $+0.16$  dex with  $\langle \sigma \rangle = 0.04$  dex and for the thin disk  $\langle [\text{Co}/\text{Fe}] \rangle = +0.06$  dex with  $\langle \sigma \rangle = 0.04$  dex, thus showing a hint of a separation.

The separation is also less distinct in the  $[\text{Ni}/\text{Fe}]$  versus  $[\text{Fe}/\text{H}]$  trend: the thick disk trend is rather flat with  $\langle [\text{Ni}/\text{Fe}] \rangle = 0.05$  dex and  $\langle \sigma \rangle = 0.03$  dex; the thin disk trend shows a slight elevation at supersolar metallicities, but the running mean remains relatively flat with  $\langle [\text{Ni}/\text{Fe}] \rangle$  about 0 dex and  $\langle \sigma \rangle = 0.03$  dex.

#### 4.2. Galactic bulge

The bulge sample consists of 45 K giants in five different fields: 11 stars in the SW field, 10 in B3, 8 in BW, 11 in B6, and 5 in BL. Jönsson et al. (2017a) concluded that a S/N below 20 has a very strong negative impact on the precision and accuracy of the determined stellar parameters and abundances. For this reason, we only used the abundances obtained from stellar spectra with S/N above 20 (about 30 stars) when calculating the running mean and  $1\sigma$  scatter. The stars with S/N below 20 are plotted in Fig. 4, but are marked differently.

In the bulge we observe one decreasing (Sc) and one increasing (Mn) trend with higher metallicity. The remaining trends of V, Cr, Co, and Ni do not change significantly as a function of  $[\text{Fe}/\text{H}]$  in the bulge.

The  $[\text{Sc}/\text{Fe}]$  value decreases from  $\sim +0.2$  dex at  $[\text{Fe}/\text{H}] \sim -0.5$  to  $\sim +0.05$  dex at  $[\text{Fe}/\text{H}] \sim +0.15$ , where it becomes flat. The average  $\langle [\text{Sc}/\text{Fe}] \rangle$  value is  $+0.1$  dex and  $\langle \sigma \rangle = 0.10$  dex. The  $[\text{V}/\text{Fe}]$  versus  $[\text{Fe}/\text{H}]$  trend decreases somewhat with higher metallicity with  $\langle [\text{V}/\text{Fe}] \rangle \sim +0.18$  dex and  $\langle \sigma \rangle = 0.09$  dex. The  $[\text{Cr}/\text{Fe}]$  value of  $\sim +0.03$  dex at  $[\text{Fe}/\text{H}] \lesssim 0$  is slightly enhanced compared to  $[\text{Cr}/\text{Fe}] \sim 0$  dex at supersolar metallicities. The  $1\sigma$  spread at  $[\text{Fe}/\text{H}] \lesssim 0$  is also significantly larger. On average the  $\langle [\text{Cr}/\text{Fe}] \rangle$  value is  $0.03$  dex and  $\langle \sigma \rangle = 0.09$  dex. The  $[\text{Mn}/\text{Fe}]$  value is steadily increasing from  $[\text{Mn}/\text{Fe}] \sim -0.15$  dex at  $[\text{Fe}/\text{H}] \sim -0.3$  to  $[\text{Mn}/\text{Fe}] \sim 0$  dex at  $[\text{Fe}/\text{H}] \sim +0.25$ . The mean  $\langle [\text{Mn}/\text{Fe}] \rangle$  value is  $-0.07$  dex and  $\langle \sigma \rangle = 0.1$  dex. The trend of Co is more or less constant with  $\langle [\text{Co}/\text{Fe}] \rangle = +0.17$  dex and  $\langle \sigma \rangle = 0.07$  dex. The  $[\text{Ni}/\text{Fe}]$  value does not change significantly with metallicity either, showing  $\langle [\text{Ni}/\text{Fe}] \rangle = +0.06$  dex and  $\langle \sigma \rangle = 0.04$  dex.

#### 4.3. Uncertainties in the determined abundances

##### 4.3.1. Systematic uncertainties

Generally, the origin of systematic errors lies in incorrectly determined stellar parameters, model atmosphere assumptions and/or atomic data, and are often quite difficult to estimate.

Abundances of the iron-peak elements examined in this work have been measured for the *Gaia* benchmark stars. These are

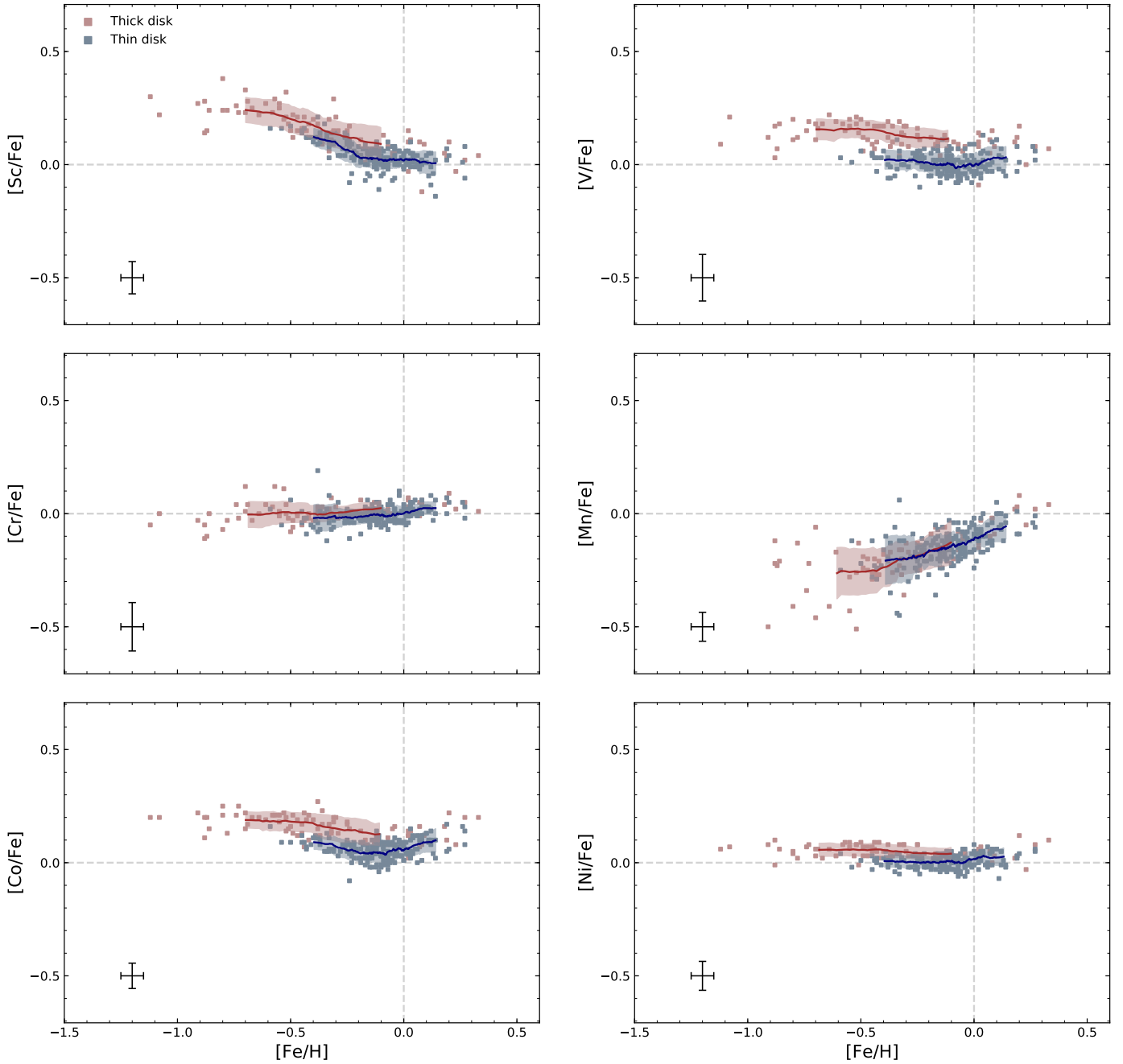


**Fig. 3.**  $[X/Fe]$  vs.  $[Fe/H]$  trends (LTE) of the examined solar neighborhood giants: pink squares denote thick disk stars and blue squares denote thin disk stars. The running mean for the thick disk is the red solid line, for the thin disk the line is blue. The shaded areas are the running  $1\sigma$  scatter of the thick (red) and thin (blue) disks. The typical uncertainties for each element from Table 2 are also shown in the plots. In the plots we use  $A(\text{Sc})_{\odot} = 3.04$  (Pehlivan Rhodin et al. 2017),  $A(\text{V})_{\odot} = 3.89$ ,  $A(\text{Cr})_{\odot} = 5.62$ ,  $A(\text{Mn})_{\odot} = 5.42$ ,  $A(\text{Fe})_{\odot} = 7.47$ ,  $A(\text{Co})_{\odot} = 4.93$ ,  $A(\text{Ni})_{\odot} = 6.20$  (Scott et al. 2015).

well-studied stars with careful stellar parameter and abundance determinations using several different methodologies (Jofré et al. 2015); three of these stars overlap with our sample:  $\alpha\text{Boo}$ ,  $\beta\text{Gem}$ , and  $\mu\text{Leo}$ . A discussion of the quality of our stellar parameters derived from the FIES spectra and other works including the benchmark values can be found in Jönsson et al. (2017a). Briefly, our parameters were found to fall within the uncertainties of the *Gaia* benchmark results, except for  $\log g$  of  $\mu\text{Leo}$  which is slightly higher.

The comparison between our determined abundances and the *Gaia* benchmark values are shown in Table 1. Our abundance results fall within the uncertainties of the benchmark values for

V and Ni. For Sc, only the abundance of  $\alpha\text{Boo}$  falls within the uncertainties of the *Gaia* benchmark values. However, we recall that we used the VALD line list for Sc, which accounts for hfs, instead of the *Gaia*-ESO list, which does not. For Cr, our results for  $\mu\text{Leo}$  and  $\alpha\text{Boo}$  fall within the uncertainties of the benchmark values, while the results for  $\beta\text{Gem}$  do not. Regarding Co, the result for  $\mu\text{Leo}$  falls within the uncertainties of the benchmark values.

The largest discrepancies are observed for Mn: 0.17, 0.34, and 0.22 dex for  $\beta\text{Gem}$ ,  $\mu\text{Leo}$ , and  $\alpha\text{Boo}$ , respectively. In the analysis we had only one satisfactory Mn line which lowers the precision of the measurements. Nevertheless, if these differences

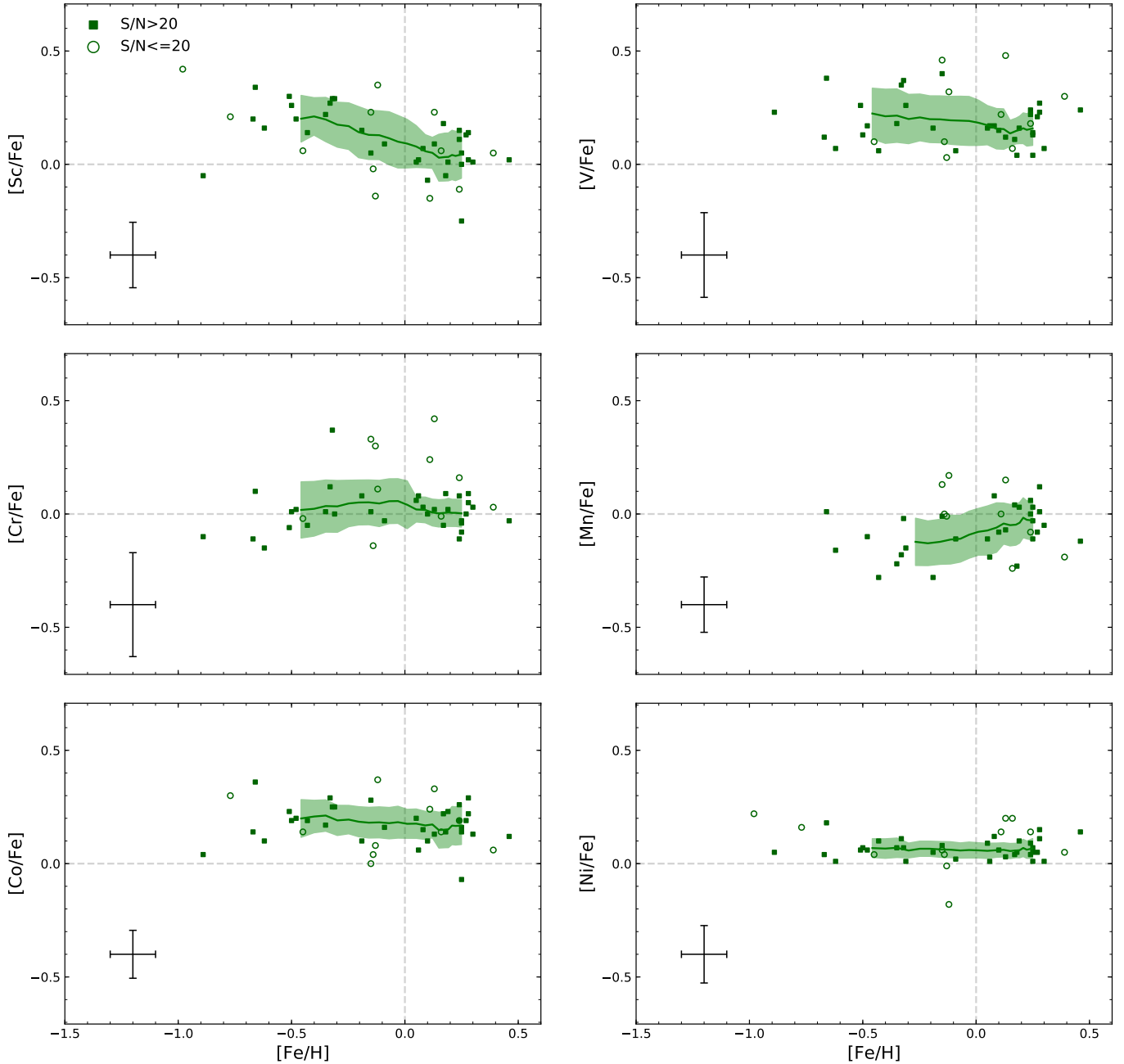


**Fig. 4.**  $[X/Fe]$  vs.  $[Fe/H]$  trends (LTE) of the examined bulge giants: green squares denote stars with spectra having a  $S/N$  above 20, while the green empty circles denote stars having spectra with an  $S/N \leq 20$ . The solid lines represent the running means and shaded areas show the  $1\sigma$  scatter (only for stars with  $S/N > 20$ ). The typical uncertainties for each element from Table 2 are also shown. In the plots we use  $A(\text{Sc})_{\odot} = 3.04$  (Pehlivan Rhodin et al. 2017),  $A(\text{V})_{\odot} = 3.89$ ,  $A(\text{Cr})_{\odot} = 5.62$ ,  $A(\text{Mn})_{\odot} = 5.42$ ,  $A(\text{Fe})_{\odot} = 7.47$ ,  $A(\text{Co})_{\odot} = 4.93$ , and  $A(\text{Ni})_{\odot} = 6.20$  (Scott et al. 2015). For spectra with  $S/N \leq 20$  the uncertainty in  $[X/Fe]$  becomes significantly large (see Jönsson et al. 2017a).

were applied to our  $[\text{Mn}/\text{Fe}]$  versus  $[\text{Fe}/\text{H}]$  trend in Fig. 3, it would become significantly lower. For example,  $\mu\text{Leo}$ , which is located at the outermost metallicity end of the Mn trend and lies at  $([\text{Fe}/\text{H}], [\text{Mn}/\text{Fe}]) = (0.23, 0.08)$ , would appear outside of the trend as low as at  $(0.23, -0.26)$ . Additionally, the benchmark values do not agree with the  $[\text{Mn}/\text{Fe}]$  versus  $[\text{Fe}/\text{H}]$  trend of F and G dwarfs from Battistini & Bensby (2015) which is presented in Sect. 5.2.1.

#### 4.3.2. Random uncertainties

Ideally, random uncertainties should be estimated for every star, but in this case, it would be very time consuming. Instead, we

followed the approach of selecting a typical star in our sample which allowed us to assign a typical random uncertainty for each abundance trend. Although fast, this method obviously cannot reflect the true uncertainty for every individual star. For example, stellar properties retrieved using spectral lines of metal poor stars are less affected by blends, but suffer more from spectral noise than lines in the spectrum of metal rich stars. Nevertheless, this method is still able to give an idea about the expected size of uncertainties in the chemical abundances.

To estimate how random uncertainties in the stellar parameters affect the measured abundances, we chose  $\alpha\text{Boo}$  to be the typical star. Our observed FIES spectrum has a high  $S/N$ , allowing us to isolate random uncertainties originating more or less

**Table 1.** Iron-peak abundances of the overlapping *Gaia* benchmark stars.

Star	$A(\text{Sc})$ (dex)	$A(\text{V})$ (dex)	$A(\text{Cr})$ (dex)	$A(\text{Mn})$ (dex)	$A(\text{Co})$ (dex)	$A(\text{Ni})$ (dex)
$\beta\text{Gem}$	$3.28 \pm 0.12$	$3.99 \pm 0.16$	$5.66 \pm 0.04$	$5.14 \pm 0.12$	$4.91 \pm 0.05$	$6.26 \pm 0.05$
HIP37826	3.09	3.92	5.73	5.31	4.98	6.24
	-0.19	-0.07	0.07	0.17	0.07	-0.02
$\mu\text{Leo}$	$3.45 \pm 0.06$	$4.23 \pm 0.06$	$5.91 \pm 0.08$	$5.39 \pm 0.20$	$5.34 \pm 0.09$	$6.50 \pm 0.12$
HIP48455	3.34	4.20	5.89	5.73	5.35	6.46
	-0.11	-0.03	-0.02	0.34	0.01	-0.04
$\alpha\text{Boo}$	$2.79 \pm 0.14$	$3.49 \pm 0.10$	$5.00 \pm 0.07$	$4.41 \pm 0.14$	$4.48 \pm 0.05$	$5.69 \pm 0.08$
HIP69673	2.66	3.41	4.95	4.63	4.56	5.64
	-0.13	-0.08	-0.05	0.22	0.08	-0.05

**Notes.** Top row: abundances presented in [Jofré et al. \(2015\)](#); middle row: our results; bottom row: difference between our results and the literature values.  $A(X) = \log\left(\frac{N_X}{N_H}\right)_* = \left[\frac{X}{H}\right]_* + \log\left(\frac{N_X}{N_H}\right)_\odot$

**Table 2.** Typical abundance uncertainties for the disk and bulge stellar samples.

Uncertainty	Sc	V	Cr	Mn	Co	Ni	Component
$\sigma_{\text{param}}$ (dex)	0.07	0.1	0.08	0.03	0.05	0.06	Disk
	0.1	0.2	0.1	0.06	0.1	0.1	Bulge
$\sigma_{\text{lbl}}$ (dex)	0.01	0.08	0.09	0.06	0.05	0.05	Disk
	0.04	0.08	0.2	0.1	0.06	0.1	Bulge
$\sigma_{\text{total}}$ (dex)	0.07	0.1	0.1	0.07	0.06	0.06	Disk
	0.2	0.2	0.2	0.1	0.1	0.1	Bulge

**Notes.**  $\sigma_{\text{param}}$  is the uncertainty due to the changes in the stellar parameters using the FIES spectrum of  $\alpha\text{Boo}$ ;  $\sigma_{\text{lbl}}$  is the uncertainty derived from the line-by-line abundance scatter for each element using the FIES spectrum of  $\alpha\text{Boo}$  (disk) and B3-f1 (bulge); and  $\sigma_{\text{total}}$  is the combined uncertainty, as in Eq. (1).

solely from the parameters. We generated a set of normally distributed random uncertainties with a standard deviation of 50 K for  $T_{\text{eff}}$ , 0.15 dex for  $\log g$ , 0.05 dex for  $[\text{Fe}/\text{H}]$ , and  $0.1 \text{ km s}^{-1}$  for  $v_{\text{mic}}$  for the disk sample. In total, 500 synthetic sets of the stellar parameters were created. These uncertainties were then added to the stellar parameters used in the original abundance measurements for  $\alpha\text{Boo}$ . The same procedure was repeated for the bulge sample, again using the stellar parameters of  $\alpha\text{Boo}$ , but the standard deviations were assumed to be twice as large as the disk.

The standard deviation obtained from the spread in abundances from the analysis of the synthetic spectra is denoted  $\sigma_{\text{param}}$  in Table 2 and shows the uncertainty in the abundances due to random uncertainties in the stellar parameters. It should be noted that this method assumes that the uncertainties are uncorrelated and produce an overestimated value. The results of the simulation for the disk and bulge are shown in Figs. B.1 and B.2.

To estimate other sources of uncertainties, we also calculated the line-by-line dispersion,  $\sigma_{\text{lbl}}$ , of the abundances for each element apart from Mn, for which only one line was analyzed. For the disk sample we again chose the FIES spectrum of  $\alpha\text{Boo}$  as the representative star, whereas for the bulge, the spectrum of B3-f1 was used as this star has typical stellar parameters and a typical S/N of  $\sim 30$ , while the S/N of the  $\alpha\text{Boo}$  spectrum is too high to represent the bulge sample. The line-by-line scatter represents a combined uncertainty originating from the continuum placement, S/N, uncertainties in  $\log gf$ -values, unknown

line blends, and shortcomings of the model atmospheres (e.g. [Johnson et al. 2014](#)). For Mn the line-by-line dispersion was assumed to be the mean of the values calculated for the other elements. This value does not include the uncertainties originating from the atomic data for the Mn I line used. We note that the disk spectra from [Thygesen et al. \(2012\)](#) have much lower S/N, and consequently larger  $\sigma_{\text{lbl}}$  than  $\alpha\text{Boo}$ . The spectra of  $\alpha\text{Boo}$  and B3-f1 from which the line-by-line abundance scatter was obtained are presented in Figs. B.3 and B.4 respectively; the  $\sigma_{\text{lbl}}$  values can be found in Table 2.

The formula for the total uncertainty,  $\sigma_{\text{total}}$ , was adapted from [Mikolaitis et al. \(2017\)](#):

$$\sigma_{\text{total}} = \sqrt{\sigma_{\text{param}}^2 + \left(\frac{\sigma_{\text{lbl}}}{\sqrt{N}}\right)^2}, \quad (1)$$

where  $\sigma_{\text{param}}$  is the uncertainty due to the stellar parameters,  $\sigma_{\text{lbl}}$  is the line-by-line dispersion and  $N$  is the number of lines used in the analysis for each element.

The typical uncertainties obtained in this way are shown in Table 2 and were used as the final uncertainty estimations.

#### 4.4. NLTE investigation

The LTE assumption might not be valid in the outer atmospheric layers of giant stars. Therefore, we discuss how NLTE corrections might alter the observed abundance trends of the iron-peak elements investigated. A departure from LTE can affect a specific

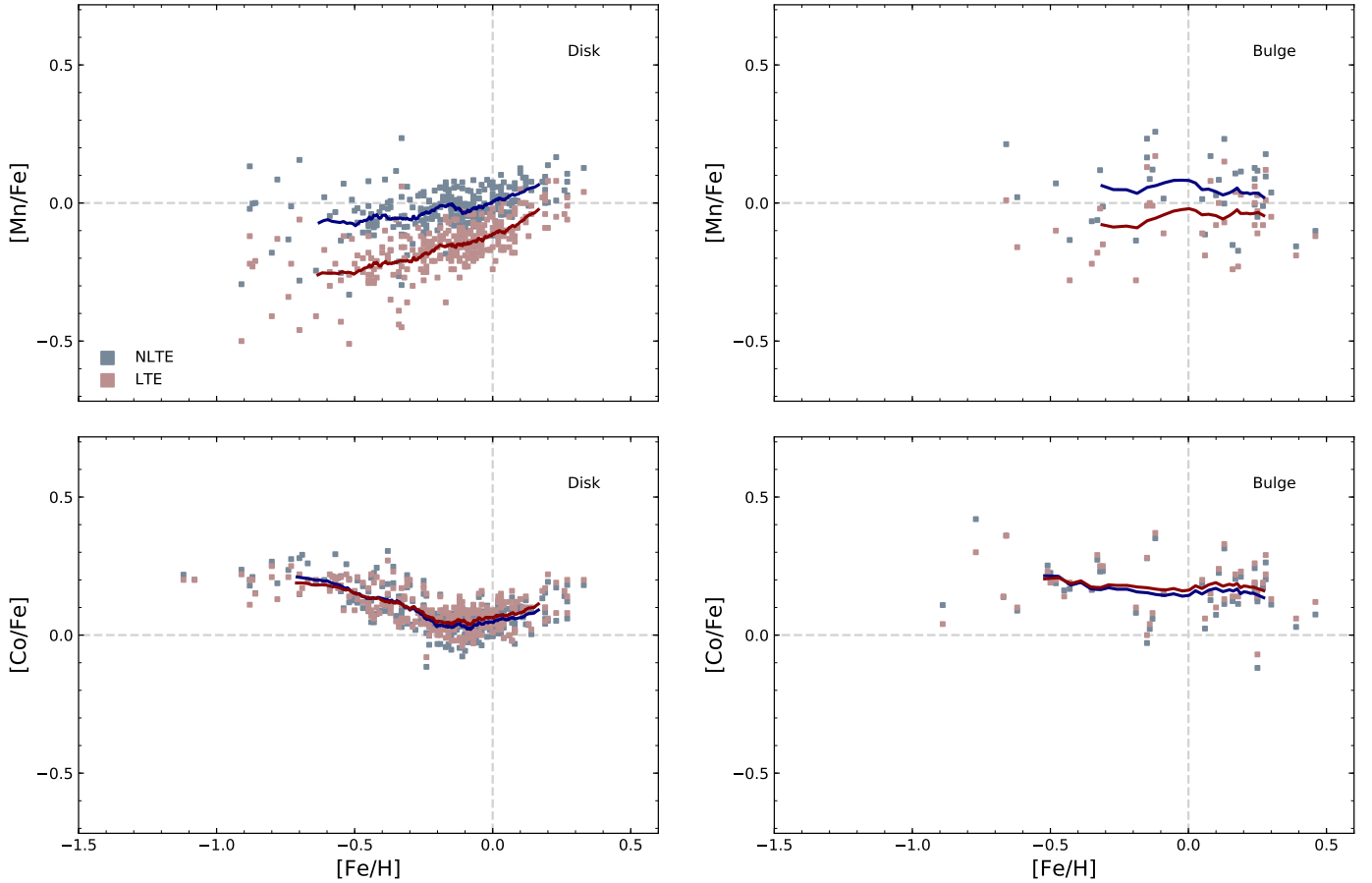


**Fig. 5.** Abundances of Mn and Co calculated for the LTE (pink) and NLTE (blue) cases in the disk (*left panels*; the thin and thick disks combined) and bulge (*right panels*). The solid lines represent the running means (LTE: red, NLTE: dark blue). The LTE/NLTE running mean of the bulge sample was calculated regardless of the S/N; therefore, the LTE running means are different from the values in Fig. 4.

line’s opacity, source function, and/or the ionization rates, and therefore the ionization balance, in the last case mostly affecting the minority species. Due to the different internal structures of giants and dwarfs, NLTE effects are likely to impact spectral lines of these stellar types differently, leading to an additional source of a systematic offset, from which giant–dwarf comparisons can suffer. Again, we note the importance of a giant–giant comparison, which reduces the offset in abundance in the given context.

The two elements for which we were able to calculate NLTE corrections are Mn and Co. The corrections were taken from Bergemann & Gehren (2008) for Mn and Bergemann et al. (2010) for Co<sup>8</sup>. We note that the corrections from Bergemann & Gehren (2008) do not account for the hyperfine splitting (hfs) of Mn I lines.

In Fig. 5, we plot NLTE and LTE abundances and running means for our two samples. Overall, the differences for [Co/Fe] are not large, and as a result, the trends remain relatively unchanged. For the trend of Mn, on the other hand, the difference is prominent and the ratio of [Mn/Fe] increases drastically, especially at low [Fe/H], and slightly flattens out in the disk and bulge.

For the remaining elements, we were not able to calculate NLTE corrections directly, however, in some cases, literature studies can give an idea about what one could expect. In the analysis, we examined lines corresponding to Sc II which is by

far the majority species in the Sun and K giants in the given temperature range ( $\sim 3900\text{--}900\text{ K}$ ). Indeed, Sc II is not as sensitive to NLTE effects as Sc I lines. Zhang et al. (2008) calculated NLTE corrections for their solar Sc II values and the differences were shown to be small ( $\Delta[\text{Sc}/\text{Fe}] = -0.03$  dex). Unfortunately, no information about NLTE corrections for giants were presented.

Previous studies of metal-poor dwarfs and giants have shown a discrepancy between abundance trends obtained from Cr I and Cr II lines: Cr I, a minority species, has a decreasing trend with decreasing metallicity compared to a rather flat trend of Cr II, a majority species (e.g. Johnson 2002; Lai et al. 2008). Bergemann & Cescutti (2010) found that this discrepancy disappears when NLTE effects are taken into account. Cr I is also a minority species in our K giants. The difference in the magnitude of NLTE corrections between the metal-rich and metal-poor stars for Cr I might be  $\sim 0.05$  dex given the results in Jofré et al. (2015). In the *Gaia* benchmark sample, the NLTE corrections for Cr I were calculated for the three overlapping stars (Jofré et al. 2015). For the metal-poor  $\alpha$  Boo ([Fe/H] =  $-0.57$ ), the NLTE abundance differs by  $+0.09$  dex from the LTE case, whereas for the more metal-rich  $\beta$  Gem ([Fe/H] =  $0.08$ ) and  $\mu$  Leo ([Fe/H] =  $0.20$ ) the corrections are  $+0.06$  and  $+0.05$  dex, respectively.

NLTE corrections for V are still not available, as discussed in Scott et al. (2015), Battistini & Bensby (2015), and Jofré et al. (2015). For our K giants, V I is a minority species, and might therefore be sensitive to NLTE effects. We are, unfortunately, unable to predict the magnitude of the NLTE corrections.

<sup>8</sup> Available online at <http://nlte.mpia.de/>

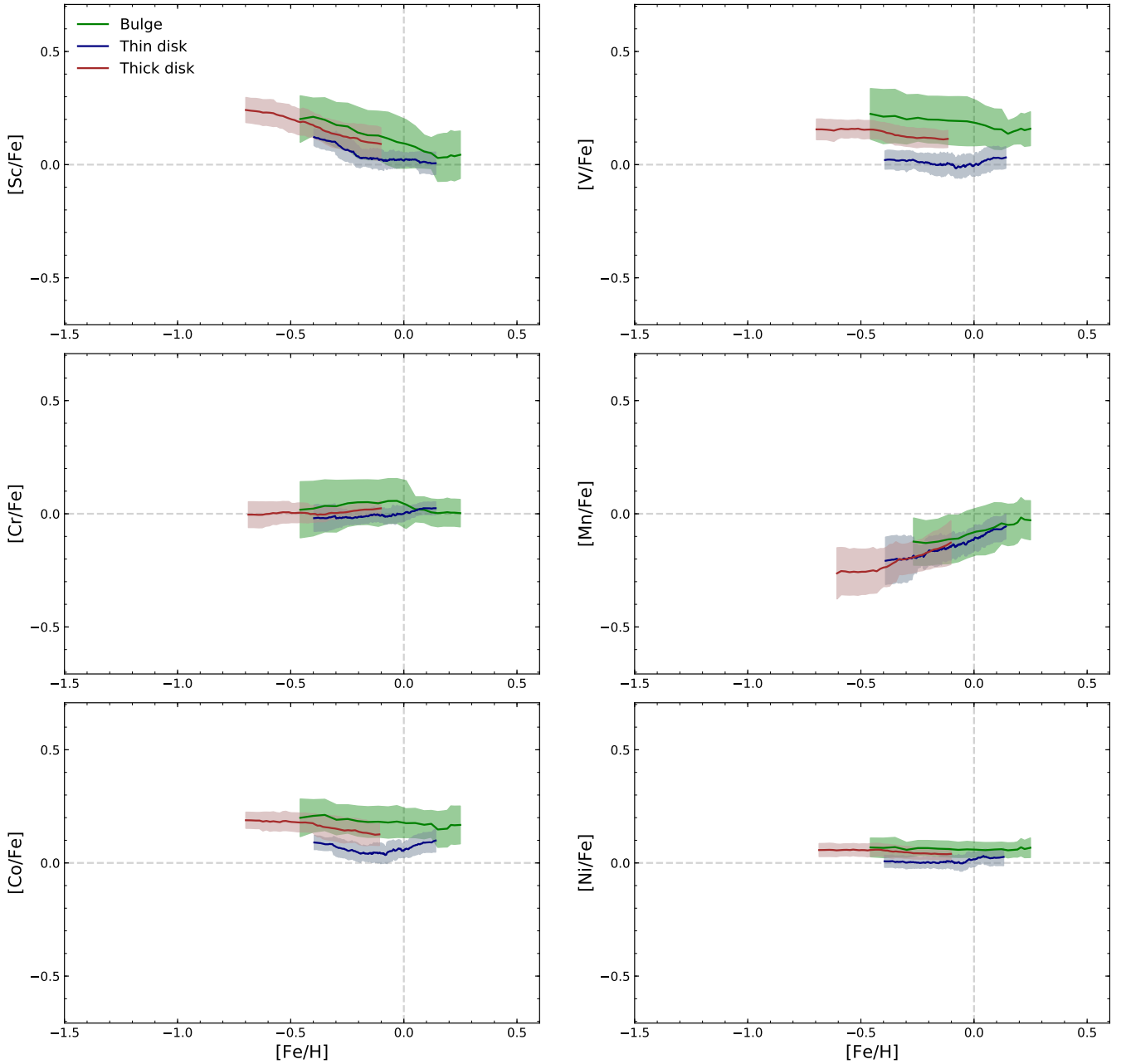


**Fig. 6.** Running means and  $1\sigma$  scatter of the thick disk (red), thin disk (blue), and bulge (green) trends (same as in Figs. 3 and 4).

Similarly to V, there are no extensive works on NLTE corrections for Ni lines (Jofré et al. 2015). However, Scott et al. (2015) argue that NLTE corrections for Ni I are probably small for the Sun in the optical region. In the case of cooler giants, Ni I is most probably the dominant species having a relatively large ionization potential.

## 5. Discussion

In this section we discuss the disk-bulge abundance trends of Sc, V, Cr, Mn, Co, and Ni and compare them to some literature studies. Again we note that this is a homogeneous giant-giant analysis of stars in the solar neighborhood and the bulge.

### 5.1. Disk and bulge: comparison

To see more clearly how the trends from the local thin and thick disks and the bulge relate to each other, we plot them together in

Fig. 6. In this plot we include the running means and running  $1\sigma$  scatter of the trends in the disk and the bulge from Figs. 3 and 4, respectively. These trends are more extensively discussed below, but to summarize, the bulge trends tend to be more enhanced than the disk trends, although with a generally high  $1\sigma$  scatter. The enhancement is largest in the trend of [V/Fe] versus [Fe/H], but it might also be enhanced in the trend of Co, although the trends' uncertainty bands mostly overlap.

#### 5.1.1. Scandium

Scandium (here and throughout we only refer to stable isotopes) is mostly produced in Ne burning or through the radioactive progenitor  $^{45}\text{Ti}$  in explosive Si and O burning (Woosley & Weaver 1995, hereafter WW95). It has a complex formation background, being predominantly produced in SNe II, similarly to  $\alpha$ -elements (e.g. Battistini & Bensby 2015), and having a dependence on the properties of the progenitor stars such as metallicity and mass

(e.g. WW95; Fig. 5 in [Nomoto et al. 2013](#) and references therein). These relations should make Sc sensitive to the environment in which it is produced.

As shown in Fig. 6, in our [Sc/Fe] versus [Fe/H] thick disk trend, there is a hint that [Sc/Fe] might be slightly more enhanced than the thin disk trend at comparable metallicities, although this is within the uncertainties. The enhancement of the thick disk in Sc has also been observed in the studies of dwarf stars in [Reddy et al. \(2003, 2006\)](#) and [Battistini & Bensby \(2015\)](#) as well as [Adibekyan et al. \(2012\)](#) up to solar metallicity. The bulge Sc trend shows a somewhat more enhanced running mean than the thick disk, and at higher [Fe/H], where only the thin disk is present, the bulge trend remains slightly enhanced with respect to the thin disk. We note, however, that the  $1\sigma$  scatter between the three trends is very prominent and non-negligible.

Present day theoretical models in [Kobayashi et al. \(2011\)](#), among others, cannot reproduce the observed Sc trends, and the formation of Sc is still poorly understood. In order to draw definite conclusions from the abundance trends of Sc, we need to better understand how it is produced. Potentially, 2D (e.g. [Maeda & Nomoto 2003](#); [Tominaga 2009](#)) and 3D ([Janka 2012](#)) models, or the  $\nu$ -process in some environments ([Iwamoto et al. 2006](#); [Heger & Woosley 2010](#); [Kobayashi et al. 2011](#)) may improve the theoretical yields in the future.

### 5.1.2. Vanadium

Vanadium is predominantly produced in explosive Si and O burning (WW95). SNe Ia are thought to create more V than SNe II do (C03), but actually little is known about the production of V. Vanadium yields produced in nucleosynthesis models do not show a strong metallicity dependence, but as in the case of Sc, they reproduce deficient [V/Fe] (e.g. [Kobayashi et al. 2011](#)).

Our V trend for the thick disk is enhanced with respect to the thin disk by approximately +0.1 dex on average, see Fig. 6. A similar enhancement of the thick disk is also observed in [Reddy et al. \(2003, 2006\)](#), [Adibekyan et al. \(2012\)](#), and [Battistini & Bensby \(2015\)](#), among others. The mean [V/Fe] of the bulge trend is quite similar to the thick disk; the average difference between them is only +0.05 dex, but the trends in Fig. 6 do not look very similar.

It is rather difficult to say what the V trend tells us about the evolution and formation of the disk and the bulge since this element is not well-explored. From our trend, we can conclude that [V/Fe] shows an enhancement in the bulge compared to the thick and thin disk. However, a significant overlap between the  $1\sigma$  scatter of the bulge and thick disk trends is present, and it increases with decreasing metallicity.

### 5.1.3. Chromium

Similarly to V, Cr is predominantly made in explosive Si and O burning (WW95). The largest yields of Cr are thought to be created in SNe Ia (C03). However, a non-negligible amount of Cr is also produced in SNe II, and given their higher frequency, the overall amount of Cr created in SNe Ia and SNe II is comparable (C03). According to some nucleosynthesis computations, Cr does not show any strong variability in SNe II and the amount produced in SNe Ia is very similar to the amount of Fe ([Kobayashi & Nakasato 2011](#)), resulting in a flat theoretical [Cr/Fe] versus [Fe/H] trend. As shown in Fig. 6, the overall disk trend of Cr does agree with the theoretical predictions apart from a possible, slight increase in [Cr/Fe] at supersolar metallicities. This elevation of the disk trend at high [Fe/H], if real,

has not been observed in [Reddy et al. \(2003\)](#), [Adibekyan et al. \(2012\)](#), and [Bensby et al. \(2014\)](#), among others. We note that the Cr I NLTE corrections for overlapping *Gaia* benchmark stars in Sect. 4.4, although they cannot be applied directly here, show a small difference between the metal-poor and metal-rich ends of the trend ( $\Delta = 0.05$  dex). Another cause for a possible elevation may be any potentially poorly modeled blends that increase with increasing metallicity. However, we have taken care to avoid using blended lines, see Sect. 3.1.

The bulge trend, on the contrary, is not flat and is enhanced at [Fe/H]  $\lesssim 0$  dex, but it decreases towards [Cr/Fe]  $\sim 0$  dex at [Fe/H]  $\gtrsim 0$  dex. This enhancement can be attributed to the larger scatter in the Cr abundance trend, as shown in Fig. 4. The overlap between the bulge and disk components is very large.

Due to a large  $1\sigma$  overlap between the disk and bulge trends that are, on average, roughly flat, we conclude that Cr is likely to be insensitive to the formation environment.

### 5.1.4. Manganese

Manganese is created in explosive Si burning and  $\alpha$ -rich freeze-out (C03). The amount of Mn produced depends, however, on the properties of the progenitor white dwarf. Computations have shown that SNe Ia events occurring at the Chandrasekhar-mass produce more Mn than Fe, independent of the metallicity of the white dwarf (e.g. [Nomoto et al. 1997](#); [Yamaguchi et al. 2015](#)). Interestingly, SNe Ia events taking place below the Chandrasekhar-mass underproduce Mn instead, but the amount of Mn increases with metallicity (e.g. [Woosley & Kasen 2011](#)). Early nucleosynthesis models indicated metallicity dependent Mn yields produced in SNe II, which proved to be very large in comparison to the yields from SNe Ia (e.g. WW95). However, more recent simulations of nucleosynthesis in SNe II produce Mn yields that are smaller at all metallicities and cannot explain the increasing [Mn/Fe] versus [Fe/H] trend without considering the SN Ia contributions ([Kobayashi et al. 2006](#); [Sukhbold et al. 2016](#)). Therefore, the main production source of Mn is presumed to be SNe Ia which makes it suitable for probing the value of SNe Ia/SNe II in different systems.

Our thin and thick disk trends for Mn in Fig. 6 strongly overlap each other, and the running means of the two trends have roughly the same slope at all metallicities. The bulge trend is marginally enhanced compared to the disk components and has a very similar slope. At the lowest metallicities, our bulge trend starts to increase, which we believe is an artificial effect due to a larger scatter. Also, as the equivalent width of the rather weak Mn I line used decreases, it becomes more sensitive to perturbations such as spectral noise and blends, lowering the precision of the measurements. As a result, the dispersion of the thick disk trend increases for [Fe/H]  $\lesssim -0.3$ . Overall, the three trends appear to be very similar.

Many studies on Mn have been carried out, and some of them have found a different behavior of the thin and thick disks. For example, [Feltzing et al. \(2007\)](#) examined disk dwarfs and concluded that the thick disk stars have a steadily increasing [Mn/Fe] with increasing [Fe/H], whereas the thin disk stars have a flat trend up to [Fe/H]  $\sim 0$  dex and an increasing trend thereafter. However, the [Mn/Fe] versus [Fe/H] trend of dwarfs in the solar neighborhood presented in [Battistini & Bensby \(2015\)](#) shows a separation that is in agreement with ours: an increasing trend with increasing [Fe/H] both in the thin and thick disk (in LTE). Similar thin and thick disk trends are also presented in [Reddy et al. \(2003, 2006\)](#) and [Adibekyan et al. \(2012\)](#). Regarding the bulge, various studies have shown an agreement between Mn

abundance trends in the bulge and the overall disk trend including the bulge giants from [Barbuy et al. \(2013\)](#) and the disk dwarfs from [Reddy et al. \(2003, 2006\)](#) (see Fig. 11 in [McWilliam \(2016\)](#) and references therein).

Based on the observed increasing  $[\text{Mn}/\text{Fe}]$  with increasing metallicity, [Gratton \(1989\)](#) suggested that Mn might be overproduced in SNe Ia compared to Fe. [McWilliam \(2016\)](#) argues that given a mere overproduction of Mn in SNe Ia, one could expect deficient  $[\text{Mn}/\text{Fe}]$  in  $\alpha$ -rich systems where the contribution from SNe II has been large, for example in the bulge. The trends of Mn in the thick disk would then also be deficient compared to the thin disk, which has only been seen in [Battistini & Bensby \(2015\)](#) when NLTE corrections from [Bergemann & Gehren \(2008\)](#) were applied resulting in a relatively flat overall disk trend. However, while the nucleosynthesis models in [Kobayashi & Nakasato \(2011\)](#) and [Nomoto et al. \(2013\)](#) can reproduce the observed LTE trends of Mn rather well, they are not able to explain the flat NLTE trend. This suggests that the NLTE corrections might not be correct (as we discussed in Sect. 4.4, the hfs was not taken into account when calculating the corrections) and/or the models might not be complete. In any case, LTE abundances of Mn, as in this work, suggest similar enrichment rates of Mn in the disk and the bulge.

#### 5.1.5. Cobalt

Cobalt is mainly created in explosive Si burning and the  $\alpha$ -rich freeze-out through the radioactive progenitor  $^{59}\text{Cu}$  and by the s-process (C03). According to the nucleosynthesis model in [Kobayashi & Nakasato \(2011\)](#) and [Kobayashi et al. \(2011\)](#), Co produces a flat trend having similar SNe yields to Cr, which is not supported by the observations. As a possible solution, [Kobayashi & Nakasato \(2011\)](#) suggest that hypernovae<sup>9</sup> (HNe) can solve the issue since they increase Co yields. [McWilliam \(2016\)](#) argues, however, that HNe, apart from producing higher Co abundances, will also result in an underabundant  $[\text{Cr}/\text{Fe}]$ , which has not been observed.

The  $[\text{Co}/\text{Fe}]$  trend in the thick disk is enhanced by  $\sim +0.1$  dex compared to the thin disk, which generally agrees with the findings in [Reddy et al. \(2003, 2006\)](#), [Adibekyan et al. \(2012\)](#), and [Battistini & Bensby \(2015\)](#). In the bulge the ratio of  $[\text{Co}/\text{Fe}]$  is higher than in the thick disk at comparable metallicities with a strong  $1\sigma$  overlap between the trends. If significant, this enhancement would suggest that the thick disk and the bulge had experienced different chemical enrichment paths. [Johnson et al. \(2014\)](#) also note a higher  $[\text{Co}/\text{Fe}]$  in the bulge than in both disk components.

#### 5.1.6. Nickel

Nickel is a product of explosive Si burning and  $\alpha$ -rich freeze-out. SNe Ia give the highest Ni yields, but SNe II, being more frequent, result in a comparable total production of Ni (C03). This element is known to produce a tight  $[\text{Ni}/\text{Fe}]$  versus  $[\text{Fe}/\text{H}]$  trend since many clean Ni lines are available in the optical region for various stellar types (e.g. [Jofré et al. 2015](#)).

Our thick disk trend is enhanced in Ni compared to the thin disk by  $\sim +0.05$  dex, which generally agrees with the findings in [Reddy et al. \(2003, 2006\)](#) and [Adibekyan et al. \(2012\)](#). The enhancement is quite small and it matches the overall

enhancement of the bulge. If true, it could be explained by assuming that the amount of SNe II nucleosynthesis products is higher in the thick disk and bulge than in the thin disk due to a higher SFR, for example. There is also a significant overlap between the  $1\sigma$  scatter of the thick disk and bulge trends. [Bensby et al. \(2017\)](#) observe a similar Ni trend in the bulge which falls on top of the thick disk trend. [Johnson et al. \(2014\)](#), on the contrary, find an enhanced Ni trend in the bulge compared to the thick disk at  $[\text{Fe}/\text{H}] \gtrsim -0.4$ , which we do not see.

### 5.2. Detailed comparison with selected literature trends

#### 5.2.1. Solar neighborhood trends by [Bensby et al. \(2014\)](#) and [Battistini & Bensby \(2015\)](#)

In this section, we compare our results to the analysis of 714 F and G dwarf and subgiant stars from the thin and thick disk in [Bensby et al. \(2014\)](#) ( $R=40\,000\text{--}110\,000$ ,  $S/N=150\text{--}300$ ,  $\lambda=\sim 3600\text{--}9300$  Å) and [Battistini & Bensby \(2015\)](#) ( $R=45\,000\text{--}120\,000$ ,  $S/N=150\text{--}300$ ,  $\lambda=\sim 3600\text{--}9300$  Å). The comparison is shown in Figs. 7 and 8. In general, the results from our giants match the results from the dwarfs, both regarding trends and scatter, but with two obvious exceptions: our  $[\text{Mn}/\text{Fe}]$  versus  $[\text{Fe}/\text{H}]$  trend is steeper, and we have an upturn in  $[\text{Co}/\text{Fe}]$  for the highest metallicities. It should be noted that due to the strictly differential analysis of the dwarfs, we do not adapt the dwarf trends to our solar values from [Scott et al. \(2015\)](#) and [Pehlivan Rhodin et al. \(2017\)](#) in Figs. 7 and 8.

For Sc, our  $[\text{Sc}/\text{Fe}]$  values follow the dwarf trend at higher metallicities down to  $[\text{Fe}/\text{H}] \sim -0.2$  dex. At  $[\text{Fe}/\text{H}] \lesssim -0.2$  our Sc trend starts to increase more rapidly with decreasing metallicity than that of the dwarfs (see Fig. 8) and follows the upper envelope of the dwarf  $[\text{Sc}/\text{Fe}]$ , as shown in Fig. 7. It is difficult to say what has caused this difference. NLTE effects are not expected to strongly affect Sc II lines as it is the majority species in K giants and FGK dwarfs.

Our V trend, on the other hand, shows an underabundance at  $[\text{Fe}/\text{H}] \lesssim -0.3$  compared to the dwarfs, as shown in Fig. 8. At  $[\text{Fe}/\text{H}] \gtrsim 0$ , our  $[\text{V}/\text{Fe}]$  becomes overabundant instead. This could potentially be due to molecular and/or atomic blends affecting our lines, which would give an metallicity dependent offset. However, it seems unlikely since we observe the same trend in all four V I lines used.

Our  $[\text{Cr}/\text{Fe}]$  shows a similar flat feature to that in [Bensby et al. \(2014\)](#) with roughly the same spread, apart from the previously discussed, possible slight increase at supersolar metallicities.

Compared to our Mn trend (LTE), the study of dwarf stars by [Battistini & Bensby \(2015\)](#) stretches out to lower metallicities, where it seems to flatten out (see Fig. 7). This behavior is expected assuming a lower contribution of Mn from SNe II dominating at earlier times (e.g. [Kobayashi et al. 2011](#)). Observation of extremely metal-poor halo stars ( $-4.0 < [\text{Fe}/\text{H}] < -2.7$ ) in [Cayrel et al. \(2004\)](#) also exhibit a similar flat trend; however, in a study of halo stars by [Honda et al. \(2004\)](#) ( $-3.1 < [\text{Fe}/\text{H}] < -2.4$ ), the  $[\text{Mn}/\text{Fe}]$  versus  $[\text{Fe}/\text{H}]$  trend is significantly scattered.

This is not the only difference between our Mn (LTE) trend and the literature. At  $[\text{Fe}/\text{H}] > 0$ , the discrepancy is smaller, but as the metallicity decreases, our trend decreases at a higher rate following the lower envelope of the dwarf trend. In the analysis, we used only one Mn I line (four lines are used in [Battistini & Bensby 2015](#)), which lowers the overall precision. Also, we note that if the *Gaia* benchmark values from Sect. 4.3.1 were adapted

<sup>9</sup> Hypernovae are very energetic (by a factor of 10 more than a regular SN II) core-collapse supernovae with masses  $M \geq 20 M_{\odot}$  ([Kobayashi et al. 2011](#)).

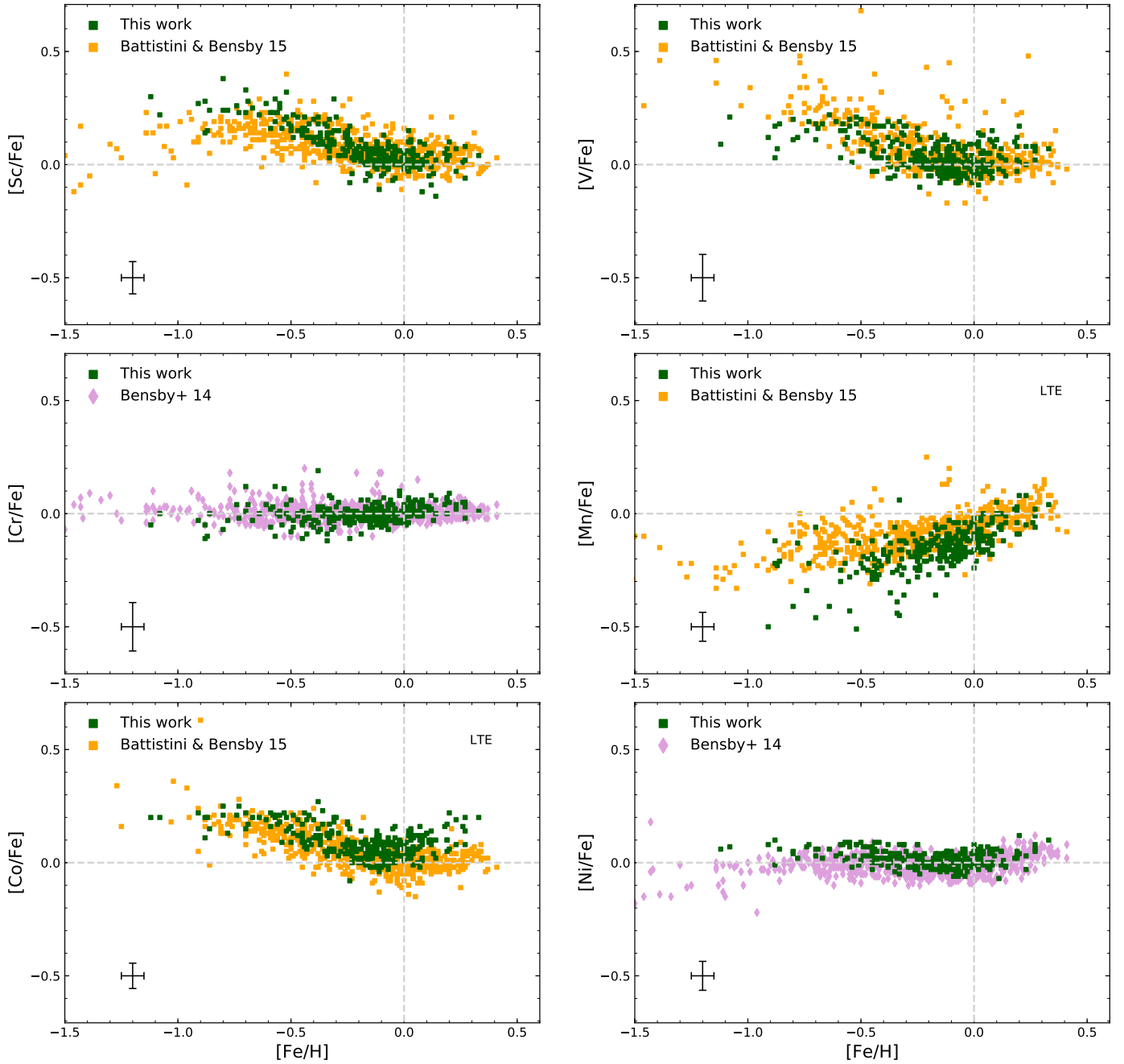


**Fig. 7.**  $[X/Fe]$  vs.  $[Fe/H]$  trends (LTE) determined for the disk giants in this work (green) together with the dwarf disk trends from Battistini & Bensby (2015) (orange) and Bensby et al. (2014) (purple). The typical uncertainties for our stars are shown as in Fig. 3.

here, the discrepancy at lower  $[Fe/H]$  would increase even more, for example the metal-poor  $\alpha$ Boo would appear at  $(-0.57, -0.44)$  instead of  $(-0.57, -0.22)$ .

When NLTE corrections are applied, the difference becomes less severe, as shown in the top row in Fig. 9. Nevertheless, our NLTE trend does not flatten out as much, although the decrease in  $[Mn/Fe]$  at low  $[Fe/H]$  could again be attributed to the larger scatter.

In Battistini & Bensby (2015), the  $[Co/Fe]$  versus  $[Fe/H]$  trend resembles the trend for Sc, having a plateau at supersolar metallicities followed by an increase with decreasing  $[Fe/H]$  which flattens out for  $[Fe/H] \lesssim -0.5$ . Up to the solar values, our  $[Co/Fe]$  versus  $[Fe/H]$  trend follows the literature values, although it is slightly enhanced, which could potentially be

connected to the choice of the solar Co abundance. As for the  $[V/Fe]$  versus  $[Fe/H]$  trend but more prominently, our  $[Co/Fe]$  values show a significant increase up to  $[Co/Fe] \sim +0.1$  dex at the supersolar metallicities. Again, one of the explanations could be atomic or molecular blends, the risk of which increases with higher  $[Fe/H]$ . However, all of the four Co I lines used in the analysis show the same increase, hence, again, line blending is unlikely to explain this upturn.

Since NLTE corrections were available for our giants and also the dwarfs in Battistini & Bensby (2015), we can check whether NLTE effects can be the reason for the discrepancy. In the bottom left panel of Fig. 9, we plot the NLTE Co abundances and in the bottom right panel we show the running mean and  $1\sigma$  scatter of the trends. As for the LTE trend of V, the trends seem to

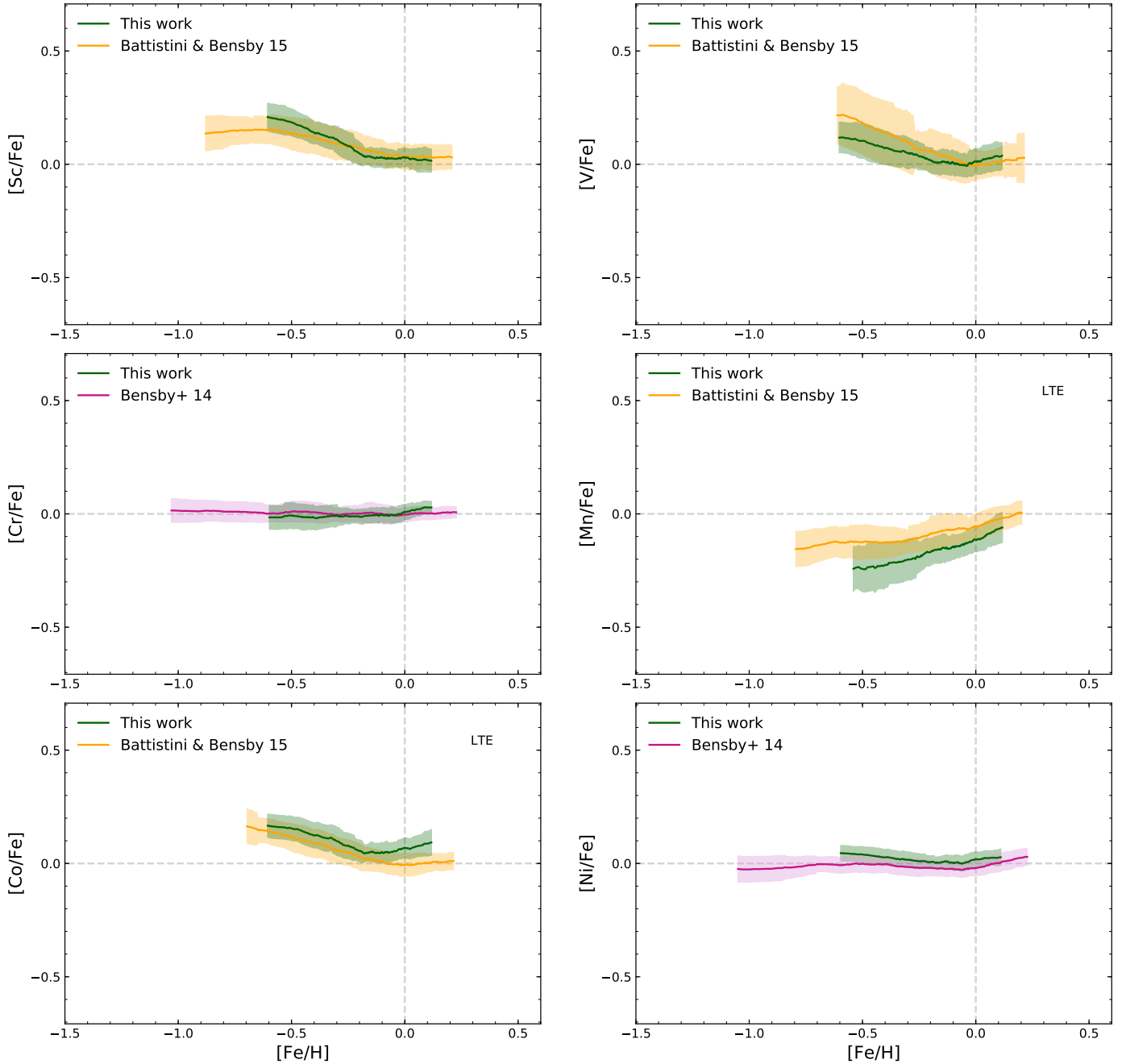


**Fig. 8.** Running means and  $1\sigma$  scatter for the disk samples (thin and thick combined) in Fig. 7: this work (green), Battistini & Bensby (2015) (orange), and Bensby et al. (2014) (purple).

be shifted in a metallicity-dependent way, which might be a sign of blending. However, the NLTE corrections applied increase the match between our trends and the reference trends, possibly indicating that the corrections applied are too small for the highest metallicities and too large for the lowest. In conclusion, we do not fully understand the origin of this divergence, and the deviation might come from the model atmospheres, which is difficult to assess.

The  $[\text{Ni}/\text{Fe}]$  versus  $[\text{Fe}/\text{H}]$  trends also show an agreement between our values and those published in Bensby et al. (2014). Our trend is somewhat enhanced, as shown in Fig. 8. This may simply be attributed to the solar Ni abundance used. Furthermore, the spreads of the two trends are similar for the metallicity range of our sample.

### 5.2.2. Galactic bulge trends

In Figs. 10 and 11 we plot the results from our investigation of the abundance trends in the bulge and a comparison with other relevant literature studies. Figure 10 shows the actual data points of all studies and their trends. Figure 11 shows the running means in order to visualize the trends more easily. We provide a thorough discussion on the comparison below, but briefly, we see that our abundance trends of the bulge mostly show a general agreement with those from the literature, although a few off-sets are discussed.

There are several high-resolution spectroscopic studies of red giants in the bulge that provide abundances of iron-peak elements. Erandes et al. (2018) ( $R = 45\,000\text{--}55\,000$ ,  $S/N = 30\text{--}300$ ,

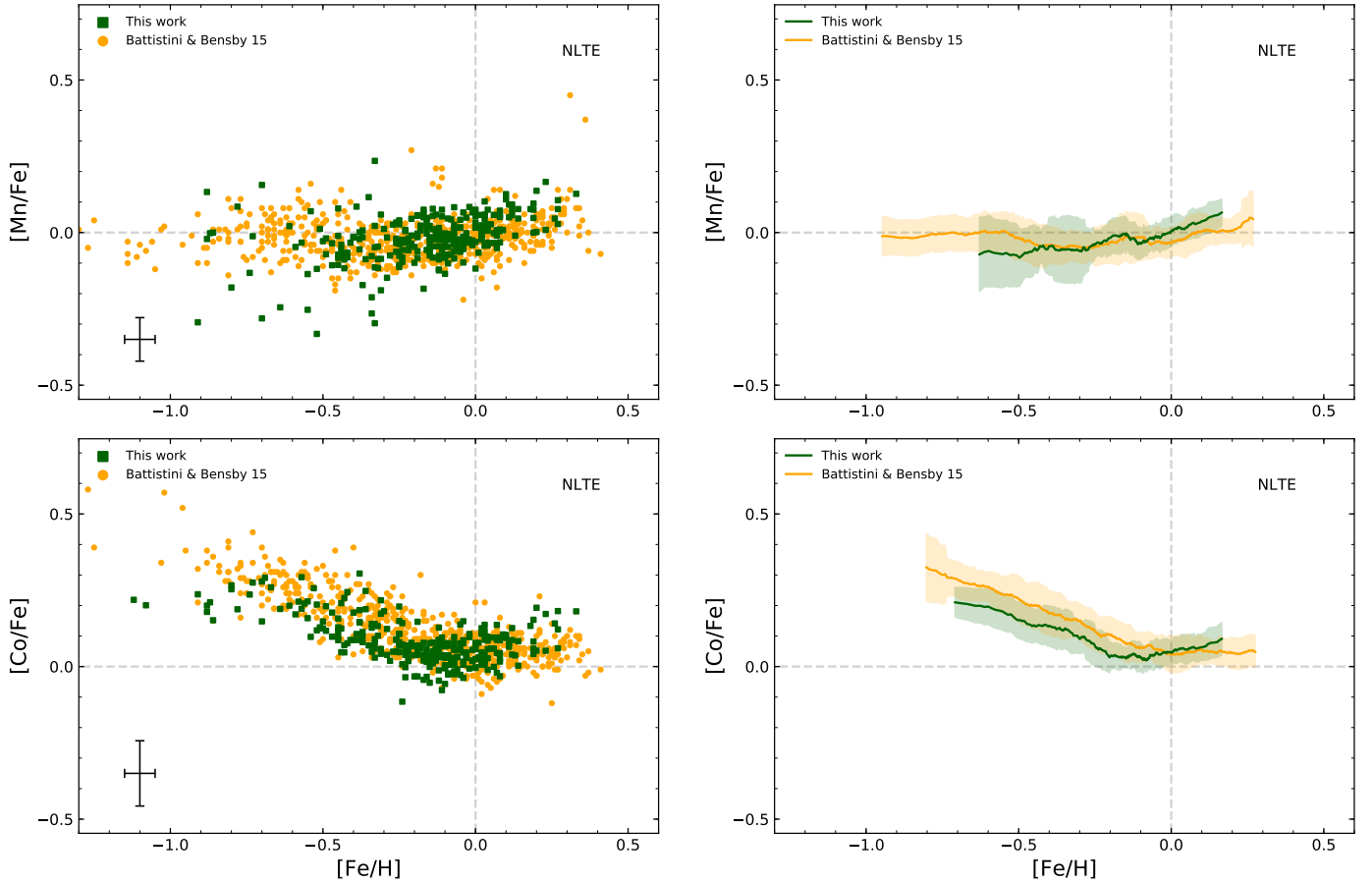


**Fig. 9.** Left panels: NLTE Mn and Co trends for our disk giants (green) and dwarfs from (Battistini & Bensby 2015) (orange). Right panels: running means and  $1\sigma$  scatter for the trends in the left panel (same colors). The typical uncertainties for our stars are shown as in Fig. 3.

$\lambda=4800\text{--}6800\text{ \AA}$ ) have studied 28 red giants in five globular clusters in the bulge and determined abundances of Sc, V, and Mn in those stars. Johnson et al. (2014) ( $R\sim 20\,000$ ,  $S/N\geq 70$ ,  $\lambda\sim 5500\text{--}7000\text{ \AA}$ ) measured abundances of Cr, Co, and Ni in 156 red giants from the Galactic bulge. Schultheis et al. (2017) ( $R=22\,500$ ,  $\lambda=1.5\text{--}1.7\text{ }\mu\text{m}$ ) worked on 269 red giants from the infra-red APOGEE survey in the Baade’s window (BW) and obtained abundances of Cr, Mn, Co, and Ni. Zasowski et al. (2019) also uses APOGEE to map the bulge over a larger area of the sky. The general abundance ratio versus metallicity trends found in Schultheis et al. (2017) are very similar to the trends in Zasowski et al. (2019), but the latter work consists of more stars. For simplicity, we have chosen to plot only the trends of Schultheis et al. (2017) in Figs. 10 and 11. Another article on Mn by Barbuy et al. (2013) ( $R=45\,000\text{--}55\,000$ ,  $S/N=9\text{--}70$ ,  $\lambda=4800\text{--}6800\text{ \AA}$ ) contains abundances of 56 red giants in the bulge. Moreover, there are 30 stars in our bulge sample that overlap with Barbuy et al. (2013). Finally, Bensby et al. (2017) ( $R=40\,000\text{--}90\,000$ ,  $S/N\sim 15\text{--}200$ ,  $\lambda\sim 3500\text{--}9500\text{ \AA}$ ) published abundances of Cr and Ni in 90 F and G dwarfs, turnoff and subgiant stars in the bulge. The locations of these stars are shown in Fig. 1, and their abundances are plotted in Figs. 10 and 11.

These authors used LTE models, and we also plot our LTE Mn and Co trend. We note that no  $S/N$  cuts were applied to the literature results. Additionally, the different works, except the results from Bensby et al. (2017) due to the differential analysis, are scaled to solar abundances used in this paper, i.e. that

of Scott et al. (2015) for all elements except Sc and of Pehlivan Rhodin et al. (2017) for Sc.

Stars from the globular clusters in Ernandes et al. (2018) stretch down to much lower metallicities, but there is an overlap in  $[\text{Fe}/\text{H}]$  with our most metal-poor giants. For Sc, V, and Mn, our results appear more enhanced compared to Ernandes et al. (2018) which is especially clear in Fig. 11. For Mn, the trend from Ernandes et al. (2018) is lower than all the other literature studies. Moreover, their  $[\text{V}/\text{Fe}]$  in the bulge are comparable to ours in the thin disk. For this reason, it appears that the results in Ernandes et al. (2018) might suffer from a systematic offset. However, the shapes of their trends are quite similar to ours in the overlapping regions.

As mentioned above, 30 of our stars were the same as the red giants from the work on Mn by Barbuy et al. (2013). However, as seen in Fig. 10, even if there are some significant abundance differences when all stars are considered, the mean value of the discrepancies between the overlapping stars is only  $-0.01$  dex with standard deviation of 0.15 dex. For the overlapping stars, Barbuy et al. (2013) adopted the stellar parameters from Zoccali et al. (2006) and Lecureur et al. (2007); the latter are discussed in Jönsson et al. (2017b). They show that the stars with the parameters from Jönsson et al. (2017b) are more spread out along the RGB in the HR-diagram and have a clearer increase in metallicity with decreasing effective temperature, which is expected from isochrones, than the stars with the parameters from Lecureur et al. (2007) (see Fig. 2 in Jönsson et al. 2017b). This suggests that the parameters used here have a higher accuracy and precision. The overall shape and position of the  $[\text{Mn}/\text{Fe}]$

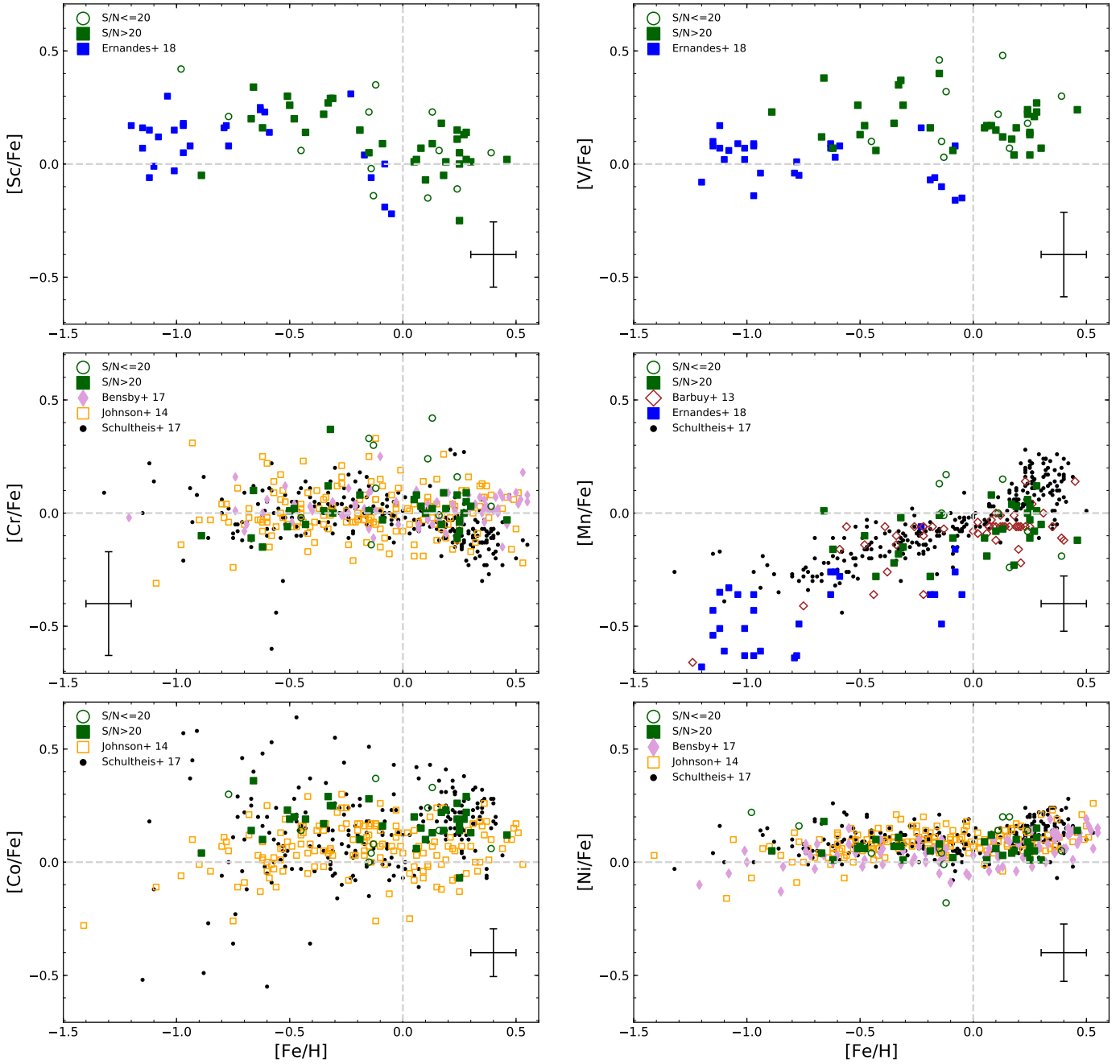


**Fig. 10.**  $[X/Fe]$  vs.  $[Fe/H]$  trends (LTE) determined for the bulge giants in this work: green squares for  $S/N$  above 20, green open circles otherwise. For spectra with  $S/N < 20$  the uncertainty in  $[X/Fe]$  becomes significantly large (see [Jönsson et al. 2017a](#)). Also plotted are bulge giant trends from [Barbuy et al. \(2013\)](#) (open red diamonds), [Ernandes et al. \(2018\)](#) (blue squares), [Johnson et al. \(2014\)](#) (open orange squares), and [Schultheis et al. \(2017\)](#) (black dots), as well as the microlensed bulge dwarfs from [Bensby et al. \(2017\)](#) (purple filled diamonds). The typical uncertainties for our stars are shown as in Fig. 4.

versus  $[Fe/H]$  trend from this work and [Barbuy et al. \(2013\)](#) are not severely affected by these differences, as seen from Figs. 10 and 11. This suggests that the Mn trend is relatively insensitive to changes in the stellar parameters. The two trends continue to rise at roughly the same rate, whereas the slope of the Mn trend in [Schultheis et al. \(2017\)](#) and [Zasowski et al. \(2019\)](#) steepens drastically at supersolar metallicities.

The disk and bulge dwarfs studied in [Bensby et al. \(2014\)](#) and [Bensby et al. \(2017\)](#) appear to have very similar Cr trends predominantly remaining at the solar value over the whole metallicity range, as seen in Figs. 8 and 11. [Johnson et al. \(2014\)](#) find a similar flat trend for their red giants. Our Cr trend seems

enhanced at  $[Fe/H] < 0$  dex; however, as discussed in Sect. 5.1.3, this is most probably due to a larger scatter between the individual stars. At  $[Fe/H] > 0$  dex, our trend converges towards  $[Cr/Fe] \sim 0$  dex as well. Interestingly, the trend from APOGEE ([Schultheis et al. 2017](#); [Zasowski et al. 2019](#)) changes from flat at  $[Fe/H] < 0$  dex to decreasing at supersolar metallicities.

Our Co trend is noticeably flatter and more enhanced than the trends in [Johnson et al. \(2014\)](#), [Schultheis et al. \(2017\)](#), and [Zasowski et al. \(2019\)](#). However, the literature trends do not fully agree either: especially in Fig. 11 we can see that the trend in [Johnson et al. \(2014\)](#) is on average slightly lower than the trend of APOGEE, and the two trend shapes are somewhat different,

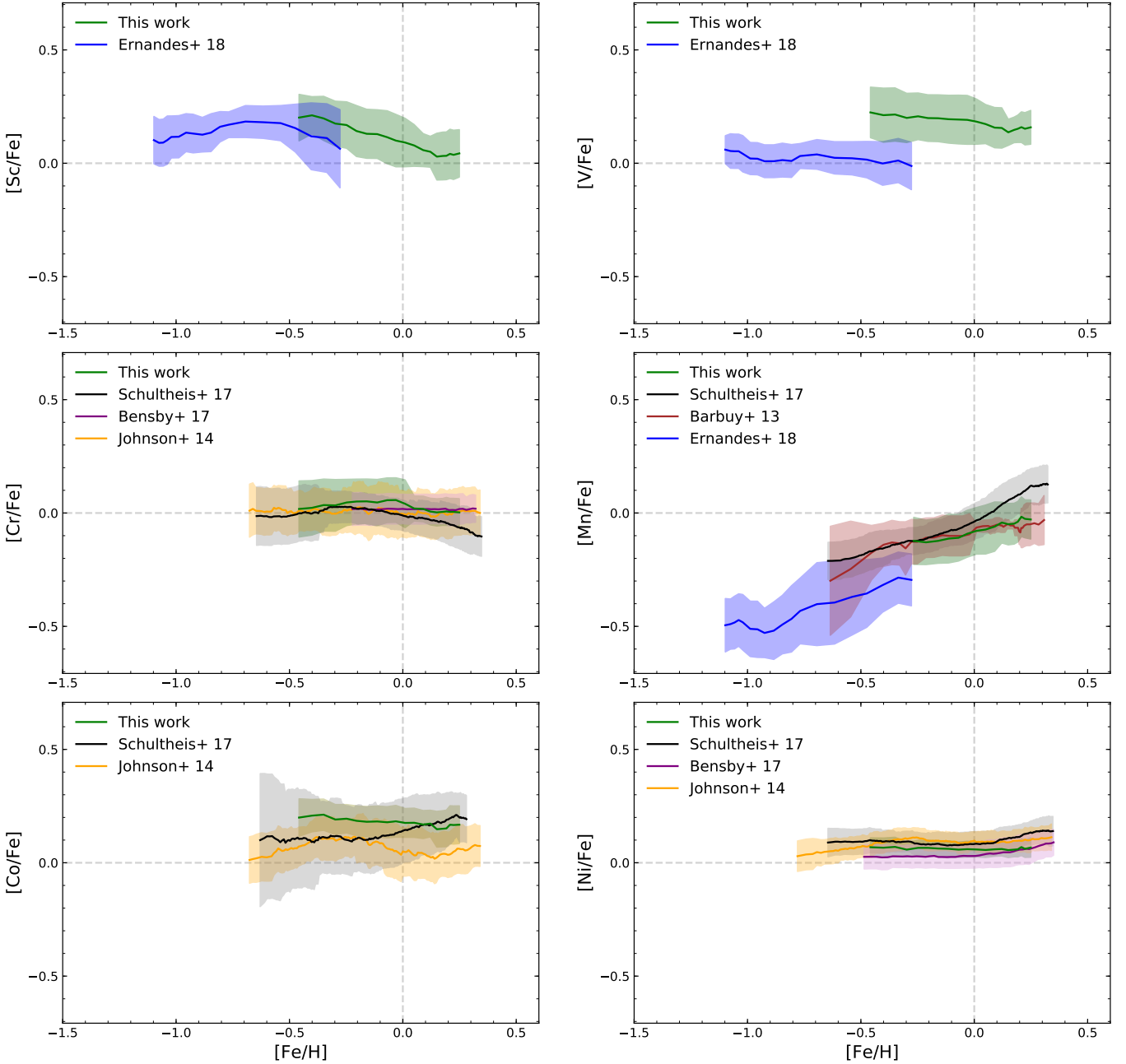


**Fig. 11.** Running means and  $1\sigma$  scatter for the bulge samples in Fig. 10: this work (green; only spectra with  $S/N > 20$ ), Barbuy et al. (2013) (red), Ernandes et al. (2018) (blue), Johnson et al. (2014) (orange), Schultheis et al. (2017) (black/grey), and Bensby et al. (2017) (purple).

too. Possibly these rather modest differences could be due to the small sample sizes in this work and in Johnson et al. (2014). It would be interesting to investigate whether a larger stellar sample would change the shape of our trend.

The trends for Ni seem to agree rather well, showing an upward feature at  $[\text{Fe}/\text{H}] > 0$  dex. The Ni trends of giants are slightly enhanced by  $\sim +0.05$  dex compared to the results in Bensby et al. (2017), which could be a question of the solar Ni abundance used: Bensby et al. (2017) perform a differential analysis against the Sun.

## 6. Conclusions

Recent observations of the bulge have revealed its boxy/peanut shape, cylindrical stellar rotation, and young stellar population, undoubtedly challenging the idea of its origin. Previously, the

bulge was thought to be a typical classical bulge formed through dissipation of gas or merging events, whereas now, in the light of the new discoveries, the idea of the secular evolution of the disk has gained more credibility. However, the true picture will almost certainly be more complicated, and apart from the disk stars, the bulge might also contain a minor spheroidal component.

In this work we provided observational constraints by measuring the abundances of six iron-peak elements (Sc, V, Cr, Mn, Co, and Ni) in K giants and performed a homogeneous giant–giant comparison of stars in the solar neighborhood and the Galactic bulge. Iron-peak elements are produced in thermonuclear and core collapse SNe, and can probe the chemical enrichment path of Galactic components, although not much attention has been paid to these elements before. We used 291 high-resolution optical spectra mainly obtained using the FIES spectrograph at the NOT for the disk sample, and 45 spectra

of bulge stars collected using the UVES/FLAMES spectrograph at the VLT. To retrieve stellar chemical compositions from the spectra, we used 1D, spherically symmetric LTE MARCS model atmospheres and the spectral synthesizer SME. The separation of the thick and thin disk components was performed using the Gaussian Mixture Model clustering method. The components were identified by the metallicity,  $[Ti/Fe]$  taken from Jönsson et al. (2017a), and by the kinematic data (proper motions and radial velocities) from *Gaia* DR2 (Gaia Collaboration 2016, 2018).

The measured abundance trends show that the thick disk is more enhanced in V and to a lesser degree in Co than the thin disk. The bulge, in turn, might be even more enhanced in V and Co than the thick disk, although within the uncertainties. We have not found any results in the literature comparing Sc and V abundances in the disk and bulge, but Johnson et al. (2014) observe an enhanced trend for the  $[Co/Fe]$  values of the bulge giants compared to the thick and thin disk dwarfs. Our  $[Ni/Fe]$  values are very similar in the thick disk and bulge, in agreement with the findings in Bensby et al. (2017), and show a strong overlap between the Ni abundances in these two trends. However, Johnson et al. (2014) find a more enhanced trend of Ni in the bulge than in the thick disk at higher  $[Fe/H]$ . For Cr, we find very similar trends in all the investigated Galactic components roughly exhibiting solar values throughout the whole metallicity range, suggesting that Cr is not sensitive to the formation environment. This has also been found in Johnson et al. (2014) and Bensby et al. (2017). The trends for Mn obtained here are again very similar in the disk and bulge being steadily increasing with increasing metallicity at about the same rate. This is consistent with the results in Barbuy et al. (2013), for example, who compare their bulge giants to, among others, the disk dwarfs in Reddy et al. (2003, 2006). The applied NLTE corrections change the  $[Mn/Fe]$  versus  $[Fe/H]$  trend drastically by enhancing it and decreasing the slope both in the disk and the bulge.

While the trends of Sc, Cr, Mn, and Ni suggest similar chemical enrichment in the bulge and local thick disk, Co and especially V exhibit some differences. Theoretical predictions cannot reproduce the observed abundance trends of V and Co in the disk (e.g. Kobayashi et al. 2011; Kobayashi & Nakasato 2011). Without having a clear idea about the production mechanisms of these elements, it is difficult to draw any definite conclusion regarding the chemical enrichment history in the disk and bulge. This issue has a complex nature since many other factors apart from the nucleosynthetic yields, such as the IMF, SFR, and gas flows, play an important role in Galactic chemical evolution models.

Based solely on the observed abundance trends of the examined iron-peak elements, we conclude that the local thick disk and the bulge might not have experienced the same evolutionary path. However, this does not necessarily contradict the fact that the Milky Way bulge is likely to have emerged through dynamical instabilities of the disk. The chemical enrichment history of the local thick disk might not be identical to that of the thick disk region closer to the bulge. A sample of thick disk stars lying closer to the Galactic center or in the inner disk is needed to confirm or reject this hypothesis.

*Acknowledgements.* We thank the anonymous referee for the insightful comments and suggestions that improved the paper in several ways. This research has been partly supported by the Lars Hierta Memorial Foundation, and the Royal Physiographic Society in Lund through Stiftelsen Walter Gyllenbergs fond and Märta och Erik Holmbergs donation. H.J. acknowledges support from the Crafoord Foundation, Stiftelsen Olle Engkvist Byggnästande, and Ruth och Nils-Stenbäckers stiftelse. This work has made use of data from the European Space Agency

(ESA) mission *Gaia* (<https://www.cosmos.esa.int/gaia>), processed by the *Gaia* Data Processing and Analysis Consortium (DPAC, <https://www.cosmos.esa.int/web/gaia/dpac/consortium>). Funding for the DPAC has been provided by national institutions, in particular the institutions participating in the *Gaia* Multilateral Agreement. This publication made use of the SIMBAD database, operated at CDS, Strasbourg, France; NASA's Astrophysics Data System; and the VALD database, operated at Uppsala University, the Institute of Astronomy RAS in Moscow, and the University of Vienna.

## References

- Abadi, M. G., Navarro, J. F., Steinmetz, M., & Eke, V. R. 2003, *ApJ*, 591, 499  
 Adibekyan, V. Z., Sousa, S. G., Santos, N. C., et al. 2012, *A&A*, 545, A32  
 Alves-Brito, A., Meléndez, J., Asplund, M., Ramírez, I., & Yong, D. 2010, *A&A*, 513, A35  
 Asplund, M., Grevesse, N., Sauval, A. J., & Scott, P. 2009, *ARA&A*, 47, 481  
 Athanassoula, E. 2005, *MNRAS*, 358, 1477  
 Babusiaux, C., Gómez, A., Hill, V., et al. 2010, *A&A*, 519, A77  
 Bailer-Jones, C. A. L., Rybizki, J., Fousneau, M., Mantelet, G., & Andrae, R. 2018, *AJ*, 156, 58  
 Barbuy, B., Hill, V., Zoccali, M., et al. 2013, *A&A*, 559, A5  
 Barbuy, B., Chiappini, C., & Gerhard, O. 2018, *ARA&A*, 56, 223  
 Battistini, C., & Bensby, T. 2015, *A&A*, 577, A9  
 Bensby, T., Alves-Brito, A., Oey, M. S., Yong, D., & Meléndez, J. 2010, *A&A*, 516, L13  
 Bensby, T., Feltzing, S., & Oey, M. S. 2014, *A&A*, 562, A71  
 Bensby, T., Feltzing, S., Gould, A., et al. 2017, *A&A*, 605, A89  
 Bergemann, M., & Gehren, T. 2008, *A&A*, 492, 823  
 Bergemann, M., & Cescutti, G. 2010, *A&A*, 522, A9  
 Bergemann, M., Pickering, J. C., & Gehren, T. 2010, *MNRAS*, 401, 1334  
 Bernard, E. J., Schultheis, M., Di Matteo, P., et al. 2018, *MNRAS*, 477, 3507  
 Blackwell-Whitehead, R., & Bergemann, M. 2007, *A&A*, 472, L43  
 Bland-Hawthorn, J., & Gerhard, O. 2016, *ARA&A*, 54, 529  
 Cardelli, J. A., Clayton, G. C., & Mathis, J. S. 1989, *ApJ*, 345, 245  
 Cardon, B. L., Smith, P. L., Scalo, J. M., Testerman, L., & Whaling, W. 1982, *ApJ*, 260, 395  
 Cayrel, R., Depagne, E., Spite, M., et al. 2004, *A&A*, 416, 1117  
 Chiappini, C., Matteucci, F., & Gratton, R. 1997, *ApJ*, 477, 765  
 Clarkson, W. I., Sahu, K. C., Anderson, J., et al. 2011, *ApJ*, 735, 37  
 Clayton, D. 2003, *Handbook of Isotopes in the Cosmos* (Cambridge: Cambridge University Press) 326  
 Combes, F., & Sanders, R. H. 1981, *A&A*, 96, 164  
 Di Matteo, P., Haywood, M., Gómez, A., et al. 2014, *A&A*, 567, A122  
 Eggen, O. J., Lynden-Bell, D., & Sandage, A. R. 1962, *ApJ*, 136, 748  
 Erandes, H., Barbuy, B., Alves-Brito, A., et al. 2018, *A&A*, 616, A18  
 Feltzing, S., Fohlman, M., & Bensby, T. 2007, *A&A*, 467, 665  
 Fragkoudi, F., Di Matteo, P., Haywood, M., et al. 2018, *A&A*, 616, A180  
 Gaia Collaboration (Prusti, T., et al.) 2016, *A&A*, 595, A1  
 Gaia Collaboration (Brown, A. G. A., et al.) 2018, *A&A*, 616, A1  
 García Pérez, A. E., Ness, M., Robin, A. C., et al. 2018, *ApJ*, 852, 91  
 Gonzalez, O. A., & Gadotti, D. 2016, *Astrophys. Space Sci. Lib.*, 418, 199  
 Gonzalez, O. A., Rejkuba, M., Zoccali, M., Valenti, E., & Minniti, D. 2011, *A&A*, 534, A3  
 Gonzalez, O. A., Rejkuba, M., Zoccali, M., et al. 2012, *A&A*, 543, A13  
 Gratton, R. G. 1989, *A&A*, 208, 171  
 Grevesse, N., Asplund, M., & Sauval, A. J. 2007, *Space Sci. Rev.*, 130, 105  
 Gustafsson, B., Edvardsson, B., Eriksson, K., et al. 2008, *A&A*, 486, 951  
 Heger, A., & Woosley, S. E. 2010, *ApJ*, 724, 341  
 Heiter, U., Lind, K., Asplund, M., et al. 2015, *Phys. Scr.*, 90, 054010  
 Hinkle, K., Wallace, L., Valenti, J., & Harmer, D. 2000, *Visible and Near Infrared Atlas of the Arcturus Spectrum 3727-9300 Å* (San Francisco: ASP), 2  
 Honda, S., Aoki, W., Kajino, T., et al. 2004, *ApJ*, 607, 474  
 Iwamoto, N., Umeda, H., Nomoto, K., et al. 2006, *Origin of Matter and Evolution of Galaxies* eds. S. Kubono, W. Aoki, T. Kajino, T. Motobayashi, & K. Nomoto, in American Institute of Physics Conference Series, 847, 409  
 Janka, H.-T. 2012, *Ann. Rev. Nucl. Part. Sci.*, 62, 407  
 Jofré, P., Heiter, U., Soubiran, C., et al. 2015, *A&A*, 582, A81  
 Johnson, J. A. 2002, *ApJS*, 139, 219  
 Johnson, C. I., Rich, R. M., Kobayashi, C., Kunder, A., & Koch, A. 2014, *AJ*, 148, 67  
 Jönsson, H., Ryde, N., Nordlander, T., et al. 2017a, *A&A*, 598, A100  
 Jönsson, H., Ryde, N., Schultheis, M., & Zoccali, M. 2017b, *A&A*, 598, A101  
 Kobayashi, C., & Nakasato, N. 2011, *ApJ*, 729, 16  
 Kobayashi, C., Umeda, H., Nomoto, K., Tominaga, N., & Ohkubo, T. 2006, *ApJ*, 653, 1145  
 Kobayashi, C., Karakas, A. I., & Umeda, H. 2011, *MNRAS*, 414, 3231  
 Kormendy, J., & Kennicutt, Jr. R. C. 2004, *ARA&A*, 42, 603

- Kunder, A., Koch, A., Rich, R. M., et al. 2012, *AJ*, **143**, 57
- Kupka, F., Piskunov, N., Ryabchikova, T. A., Stempels, H. C., & Weiss, W. W. 1999, *A&AS*, **138**, 119
- Kurucz, R. L. 2009, [Robert L. Kurucz on-line database of observed and predicted atomic transitions](#)
- Kurucz, R. L. 2010, [Robert L. Kurucz on-line database of observed and predicted atomic transitions](#)
- Lai, D. K., Bolte, M., Johnson, J. A., et al. 2008, *ApJ*, **681**, 1524
- Lawler, J. E., & Dakin, J. T. 1989, *J. Opt. Soc. Am. B: Opt. Phys.*, **6**, 1457
- Lecureur, A., Hill, V., Zoccali, M., et al. 2007, *A&A*, **465**, 799
- Lind, K., Bergemann, M., & Asplund, M. 2012, *MNRAS*, **427**, 50
- Lütticke, R., Dettmar, R.-J., & Pohlen, M. 2000, *A&AS*, **145**, 405
- Maeda, K., & Nomoto, K. 2003, *ApJ*, **598**, 1163
- Marquardt, D. W. 1963, *SIAM J. Appl. Math.*, **11**, 431
- Martinez-Valpuesta, I., Shlosman, I., & Heller, C. 2006, *ApJ*, **637**, 214
- Matteucci, F. 2012, *Chemical Evolution of Galaxies* (Berlin: Springer-Verlag) 226
- McWilliam, A. 2016, *PASA*, **33**, e040
- McMillan, P. J. 2018, *RNAAS*, **2**, 51
- McWilliam, A., & Zoccali, M. 2010, *ApJ*, **724**, 1491
- Meléndez, J., Asplund, M., Alves-Brito, A., et al. 2008, *A&A*, **484**, L21
- Micali, A., Matteucci, F., & Romano, D. 2013, *MNRAS*, **436**, 1648
- Mikolaitis, Š., de Laverny, P., Recio-Blanco, A., et al. 2017, *A&A*, **600**, A22
- Nandakumar, G., Ryde, N., Schultheis, M., et al. 2018, *MNRAS*, **478**, 4374
- Nataf, D. M., Udalski, A., Gould, A., Fouqué, P., & Stanek, K. Z. 2010, *ApJ*, **721**, L28
- Ness, M., Freeman, K., Athanassoula, E., et al. 2013, *MNRAS*, **432**, 2092
- Ness, M., Hogg, D. W., Rix, H.-W., et al. 2016, *ApJ*, **823**, 114
- Nissen, P. E. 2004, *Origin and Evolution of the Elements*, (Cambridge: Cambridge University Press), 154
- Nomoto, K., Iwamoto, K., Nakasato, N., et al. 1997, *Nucl. Phys. A*, **621**, 467
- Nomoto, K., Kobayashi, C., & Tominaga, N. 2013, *ARA&A*, **51**, 457
- Pakhomov, Y., Piskunov, N., & Ryabchikova, T. 2017, in *Stars: From Collapse to Collapse*, eds. Y. Y. Balega, D. O. Kudryavtsev, I. I. Romanyuk, & I. A. Yakunin, *ASP Conf. Ser.*, **510518**
- Pedregosa, F., Varoquaux, G., Gramfort, A., et al. 2011, *J. Mach. Learn. Res.*
- Pehlivan Rhodin, A., Belmonte, M. T., Engström, L., et al. 2017, *MNRAS*, **472**, 3337
- Petit, P., Louge, T., Théado, S., et al. 2014, *PASP*, **126**, 469
- Piskunov, N., & Valenti, J. A. 2017, *A&A*, **597**, A16
- Prochaska, J. X., & McWilliam, A. 2000, *ApJ*, **537**, L57
- Reddy, B. E., Tomkin, J., Lambert, D. L., & Allende Prieto, C. 2003, *MNRAS*, **340**, 304
- Reddy, B. E., Lambert, D. L., & Allende Prieto, C. 2006, *MNRAS*, **367**, 1329
- Reynolds, D. A. 2009, *Encyclopedia of Biometrics* (Boston: Springer)
- Rich, R. M., Origlia, L., & Valenti, E. 2012, *ApJ*, **746**, 59
- Rich, R. M., Ryde, N., Thorsbro, B., et al. 2017, *AJ*, **154**, 239
- Ryde, N., Fritz, T. K., Rich, R. M., et al. 2016, *ApJ*, **831**, 40
- Scannapieco, C., & Tissera, P. B. 2003, *MNRAS*, **338**, 880
- Schultheis, M., Ryde, N., & Nandakumar, G. 2016, *A&A*, **590**, A6
- Schultheis, M., Rojas-Arriagada, A., García Pérez, A. E., et al. 2017, *A&A*, **600**, A14
- Scott, P., Asplund, M., Grevesse, N., Bergemann, M., & Sauval, A. J. 2015, *A&A*, **573**, A26
- Shen, J., Rich, R. M., Kormendy, J., et al. 2010, *ApJ*, **720**, L72
- Snedden, C., Cowan, J. J., Kobayashi, C., et al. 2016, *ApJ*, **817**, 53
- Sobeck, J. S., Lawler, J. E., & Sneden, C. 2007, *ApJ*, **667**, 1267
- Sukhbold, T., Ertl, T., Woosley, S. E., Brown, J. M., & Janka, H.-T. 2016, *ApJ*, **821**, 38
- Telting, J. H., Avila, G., Buchhave, L., et al. 2014, *Astron. Nachr.*, **335**, 41
- Thorsbro, B., Ryde, N., Schultheis, M., et al. 2018, *ApJ*, **866**, 52
- Thygesen, A. O., Frandsen, S., Bruntt, H., et al. 2012, *A&A*, **543**, A160
- Tominaga, N. 2009, *ApJ*, **690**, 526
- Valenti, J. A., & Piskunov, N. 1996, *A&AS*, **118**, 595
- van Loon, J. T., Gilmore, G. F., Omont, A., et al. 2003, *MNRAS*, **338**, 857
- Vásquez, S., Zoccali, M., Hill, V., et al. 2013, *A&A*, **555**, A91
- Wegg, C., & Gerhard, O. 2013, *MNRAS*, **435**, 1874
- Wegg, C., Gerhard, O., & Portail, M. 2015, *MNRAS*, **450**, 4050
- Weiland, J. L., Arendt, R. G., Berriman, G. B., et al. 1994, *ApJ*, **425**, L81
- Whaling, W., Hannaford, P., Lowe, R. M., Biemont, E., & Grevesse, N. 1985, *A&A*, **153**, 109
- Wood, M. P., Lawler, J. E., Sneden, C., & Cowan, J. J. 2014, *ApJS*, **211**, 20
- Woosley, S. E., & Weaver, T. A. 1995, *ApJS*, **101**, 181
- Woosley, S. E., & Kasen, D. 2011, *ApJ*, **734**, 38
- Yamaguchi, H., Badenes, C., Foster, A. R., et al. 2015, *ApJ*, **801**, L31
- Zasowski, G., Ness, M. K., García Pérez, A. E., et al. 2016, *ApJ*, **832**, 132
- Zasowski, G., Schultheis, M., Hasselquist, S., et al. 2019, *ApJ*, **870**, 138
- Zhang, H. W., Gehren, T., & Zhao, G. 2008, *A&A*, **481**, 489
- Zoccali, M., Lecureur, A., Barbuy, B., et al. 2006, *A&A*, **457**, L1
- Zoccali, M., Vasquez, S., Gonzalez, O. A., et al. 2017, *A&A*, **599**, A12

**Appendix A: Additional tables****Table A.1.** Basic data for the observed solar neighborhood giants.

HIP/KIC/TYC	Alternative name	RA (J2000) (h:m:s)	Dec (J2000) (d:am:as)	$V$	$v_{\text{rad}}$ $\text{km s}^{-1}$	$S/N$	Source
HIP1692	HD 1690	00:21:13.32713	-08:16:52.1625	9.18	18.37	114	FIES-archive
HIP9884	alfAri	02:07:10.40570	+23:27:44.7032	2.01	-14.29	90	PolarBase
HIP10085	HD 13189	02:09:40.17260	+32:18:59.1649	7.56	26.21	156	FIES-archive
HIP12247	81Cet	02:37:41.80105	-03:23:46.2201	5.66	9.34	176	FIES-archive
HIP28417	HD 40460	06:00:06.03883	+27:16:19.8614	6.62	100.64	121	PolarBase
HIP33827	HR 2581	07:01:21.41827	+70:48:29.8674	5.69	-17.99	79	PolarBase
HIP35759	HD 57470	07:22:33.85798	+29:49:27.6626	7.67	-30.19	85	PolarBase
HIP37447	alfMon	07:41:14.83257	-09:33:04.0711	3.93	11.83	71	Thygesen et al. (2012)
HIP37826	betGem	07:45:18.94987	+28:01:34.3160	1.14	3.83	90	PolarBase
HIP43813	zetHya	08:55:23.62614	+05:56:44.0354	3.10	23.37	147	PolarBase

**Notes.** Coordinates and magnitudes are taken from the SIMBAD database, while the radial velocities are measured from the spectra. The  $S/N$  per data point is measured by the IDL-routine `der_snr.pro`, see [http://www.stecf.org/software/ASTROsoft/DER\\_SNR](http://www.stecf.org/software/ASTROsoft/DER_SNR). This is only an excerpt of the table to show its form and content. The complete table is available at the CDS.

**Table A.2.** Basic data for the observed bulge giants.

Star <sup>(a)</sup>	RA (J2000) (h:m:s)	Dec (J2000) (d:am:as)	$V$	$S/N$
SW-09	17:59:04.533	-29:10:36.53	16.153	16
SW-15	17:59:04.753	-29:12:14.77	16.326	15
SW-17	17:59:08.138	-29:11:20.10	16.388	11
SW-18	17:59:06.455	-29:10:30.53	16.410	14
SW-27	17:59:04.457	-29:10:20.67	16.484	13
SW-28	17:59:07.005	-29:13:11.35	16.485	16
SW-33	17:59:03.331	-29:10:25.60	16.549	14
SW-34	17:58:54.418	-29:11:19.82	16.559	12
SW-43	17:59:04.059	-29:13:30.26	16.606	16
SW-71	17:58:58.257	-29:12:56.97	16.892	14

**Notes.** The  $S/N$  per data point is measured by the IDL-routine `der_snr.pro`, see [http://www.stecf.org/software/ASTROsoft/DER\\_SNR](http://www.stecf.org/software/ASTROsoft/DER_SNR). This is only an excerpt of the table to show its form and content. The complete table is available at the CDS. <sup>(a)</sup>Using the same naming convention as Lecureur et al. (2007) for the B3-BW-B6-BL-stars.

**Table A.3.** Atomic data for the spectral lines used in the analysis.

Element	Wavelength (Å) (air)	$\log gf$	$\chi_{\text{exc}}$ (eV)	Reference
Sc II	6245.6205	-1.624	1.50695	1
Sc II	6245.6290	-2.364	1.50695	1
Sc II	6245.6309	-1.795	1.50695	1
Sc II	6245.6362	-3.364	1.50695	1
Sc II	6245.6380	-2.181	1.50695	1
Sc II	6245.6396	-2.002	1.50695	1
Sc II	6245.6438	-2.946	1.50695	1
Sc II	6245.6454	-2.148	1.50695	1
Sc II	6245.6468	-2.273	1.50695	1
Sc II	6245.6499	-2.712	1.50695	1

**Notes.** All atomic data apart from Sc were collected by the *Gaia*-ESO line list group (Heiter et al. 2015). For Sc atomic data are from the VALD list (Kupka et al. 1999; Pakhomov et al. 2017). The references listed are for  $\log gf$ . This is only an excerpt of the table to show its form and content. The complete table is available at the CDS.

**References.** (1) Kurucz (2009), (2) Lawler & Dakin (1989), (3) Whaling et al. (1985), (4) Sobek et al. (2007), (5) Kurucz (2010), (6) Blackwell-Whitehead & Bergemann (2007), (7) Cardon et al. (1982), (8) Wood et al. (2014).

**Table A.4.** Stellar parameters and determined abundances for observed solar neighborhood giants.

HIP/KIC/TYC	$T_{\text{eff}}$	$\log g$	[Fe/H]	$v_{\text{mic}}$	A(Sc)	A(V)	A(Cr)	A(Mn)	A(Co)	A(Ni)
HIP1692	4216	1.79	-0.26	1.55	2.90	3.68	5.32	4.99	...	5.98
HIP9884	4464	2.27	-0.21	1.34	2.90	3.70	5.42	5.05	...	5.98
HIP10085	4062	1.44	-0.32	1.63	2.81	3.57	5.23	4.90	...	5.90
HIP12247	4790	2.71	-0.04	1.40	3.00	3.81	5.58	5.20	...	6.14
HIP28417	4746	2.56	-0.25	1.40	2.92	3.68	5.38	4.96	...	5.97
HIP33827	4235	1.99	0.01	1.50	3.05	3.90	5.62	5.34	...	6.23
HIP35759	4606	2.47	-0.15	1.42	2.92	3.78	5.47	5.10	...	6.07
HIP37447	4758	2.73	-0.04	1.35	3.04	3.80	5.60	5.21	...	6.14
HIP37826	4835	2.93	0.07	1.24	3.09	3.92	5.73	5.31	4.98	6.24
HIP43813	4873	2.62	-0.07	1.51	2.98	3.78	5.59	5.16	4.83	6.07

**Notes.** [Fe/H] is listed in the scale of [Scott et al. \(2015\)](#). This is only an excerpt of the table to show its form and content. The complete table is available at the CDS.

**Table A.5.** Stellar parameters and determined abundances for observed bulge giants.

Star	$T_{\text{eff}}$	$\log g$	[Fe/H]	$v_{\text{mic}}$	A(Sc)	A(V)	A(Cr)	A(Mn)	A(Co)	A(Ni)
SW-09	4095	1.79	-0.15	1.32	3.12	4.20	5.80	5.40	4.78	6.11
SW-15	4741	1.96	-0.98	1.62	2.48	...	...	...	...	5.44
SW-17	4245	2.09	0.24	1.44	3.17	4.31	6.02	5.58	5.36	6.58
SW-18	4212	1.67	-0.13	1.49	2.77	3.79	5.79	5.28	4.88	6.06
SW-27	4423	2.34	0.11	1.60	3.00	4.22	5.97	5.53	5.28	6.45
SW-28	4254	2.36	-0.14	1.44	2.88	3.85	5.34	5.28	4.83	6.10
SW-33	4580	2.72	0.16	1.39	3.26	4.12	5.77	5.34	5.23	6.56
SW-34	4468	1.75	-0.45	1.63	2.65	3.54	5.15	...	4.62	5.79
SW-43	4892	2.34	-0.77	1.84	2.48	...	...	...	4.46	5.59
SW-71	4344	2.66	0.39	1.31	3.48	4.58	6.04	5.62	5.38	6.64

**Notes.** [Fe/H] is listed in the scale of [Scott et al. \(2015\)](#). This is only an excerpt of the table to show its form and content. The complete table is available at the CDS.

## Appendix B: Additional figures

Panels a and c in the first and fourth rows in Figs. B.3 and B.4 show a strongly overestimated synthetic spectrum (red) of two

V I lines. This divergence is most likely the result of imprecise  $\log gf$  values for these lines. These lines have not been used in the analysis, and they do not affect the fits and measurements done for the lines of interest, i.e. the adjacent Sc and Co lines.

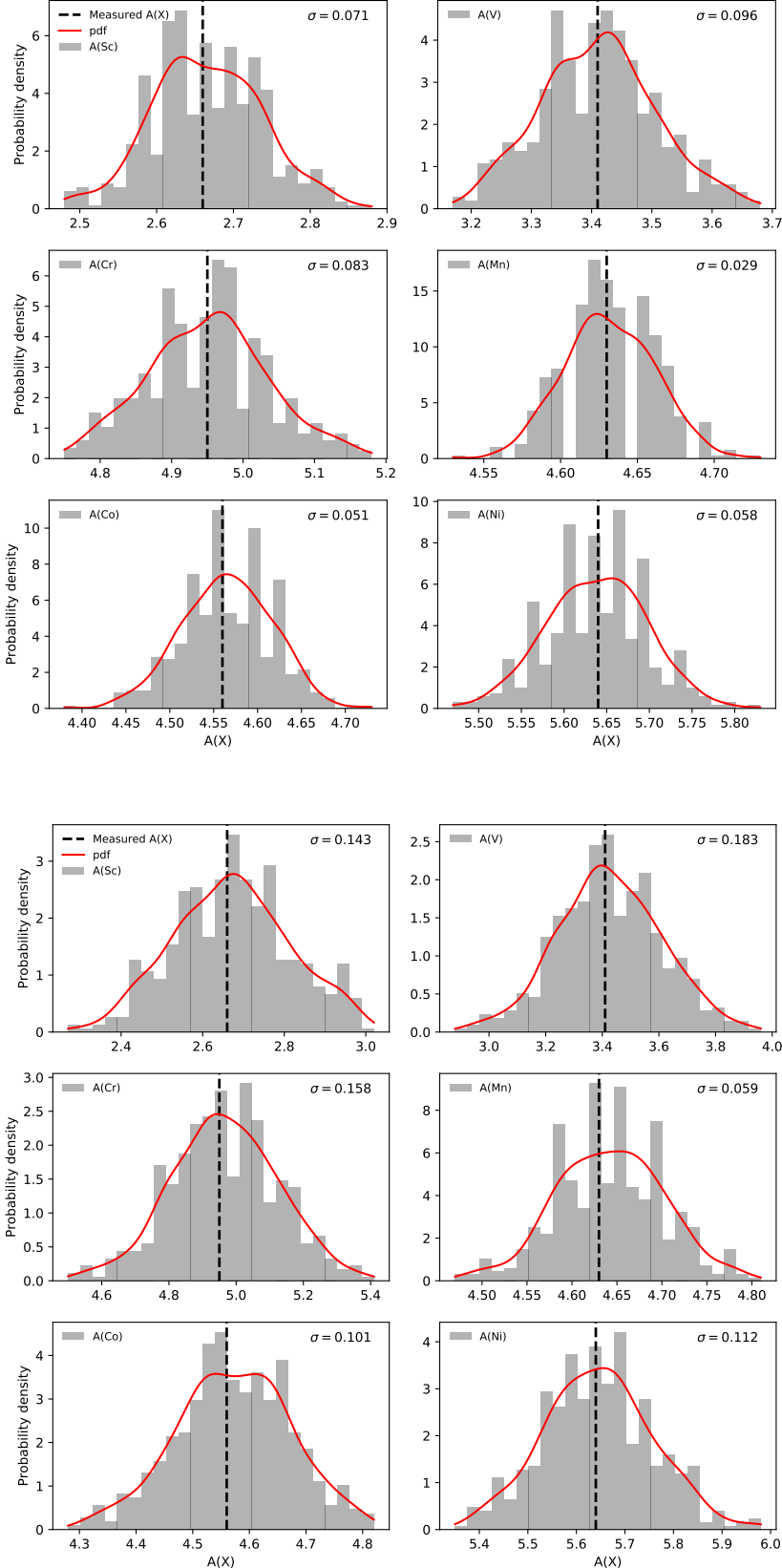


**Fig. B.1.** Histograms of the abundances determined from 500 synthetic data sets using the spectrum  $\alpha$ Boo for the disk sample. The red line denotes the estimated probability density function for each element, and  $\sigma$  is the standard deviation of each synthetic sample.

**Fig. B.2.** Histograms of the abundances determined from 500 synthetic data sets using the spectrum  $\alpha$ Boo for the bulge sample. The red line denotes the estimated probability density function for each element, and  $\sigma$  is the standard deviation of each synthetic sample.

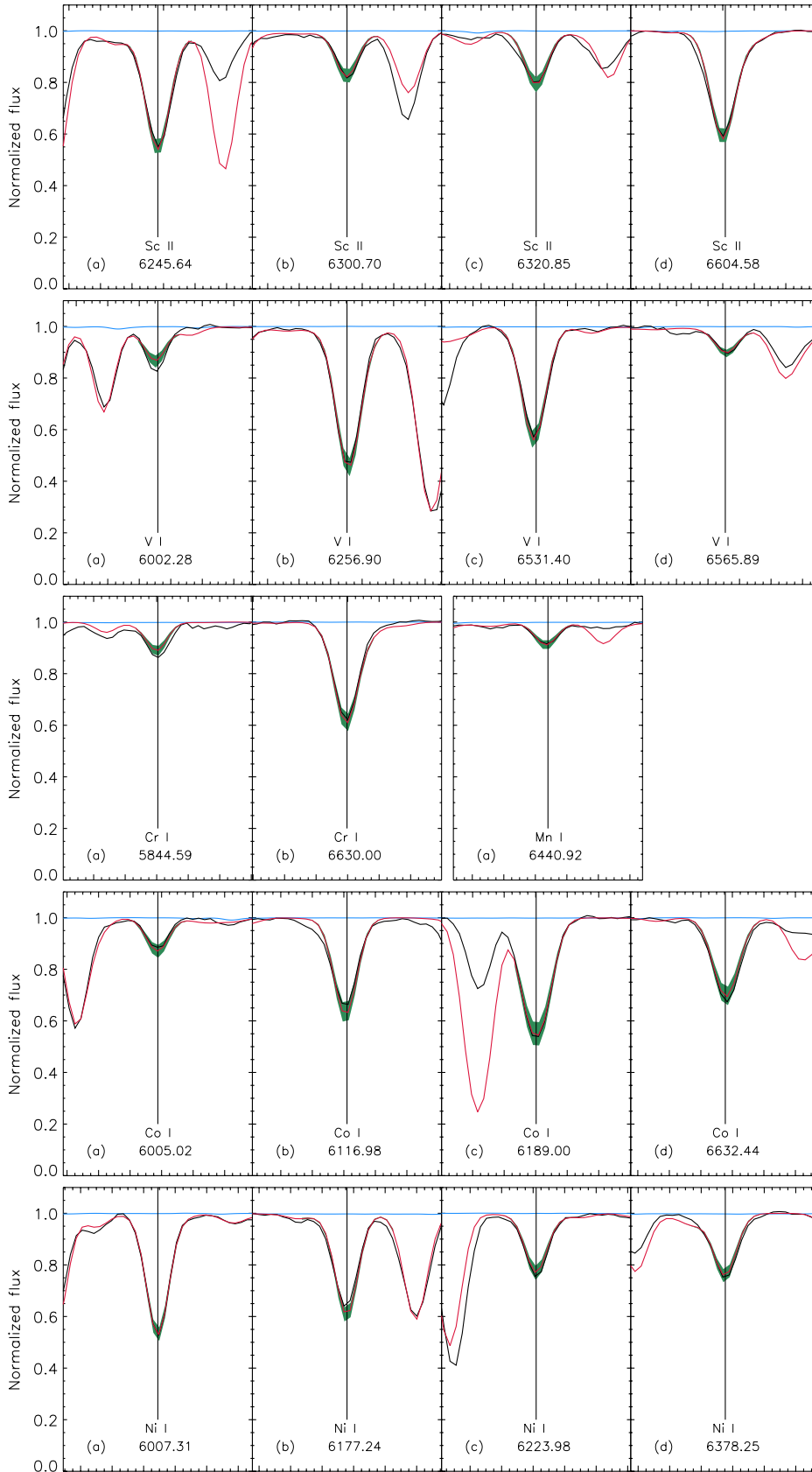


**Fig. B.3.** Stellar lines used for the calculations of the line-by-line abundance scatter and for the abundance determination in the analysis in the spectrum of  $\alpha$ Boo. The black line is the observed spectrum, the red line is the fitted spectrum, and the blue line is the telluric spectrum from the  $\alpha$ Boo atlas of Hinkle et al. (2000); in green is  $\pm 0.2$  dex of the element in question. The wavelength range of each panel is  $1.2 \text{ \AA}$ , i.e. the large tickmarks correspond to steps of  $0.2 \text{ \AA}$ .

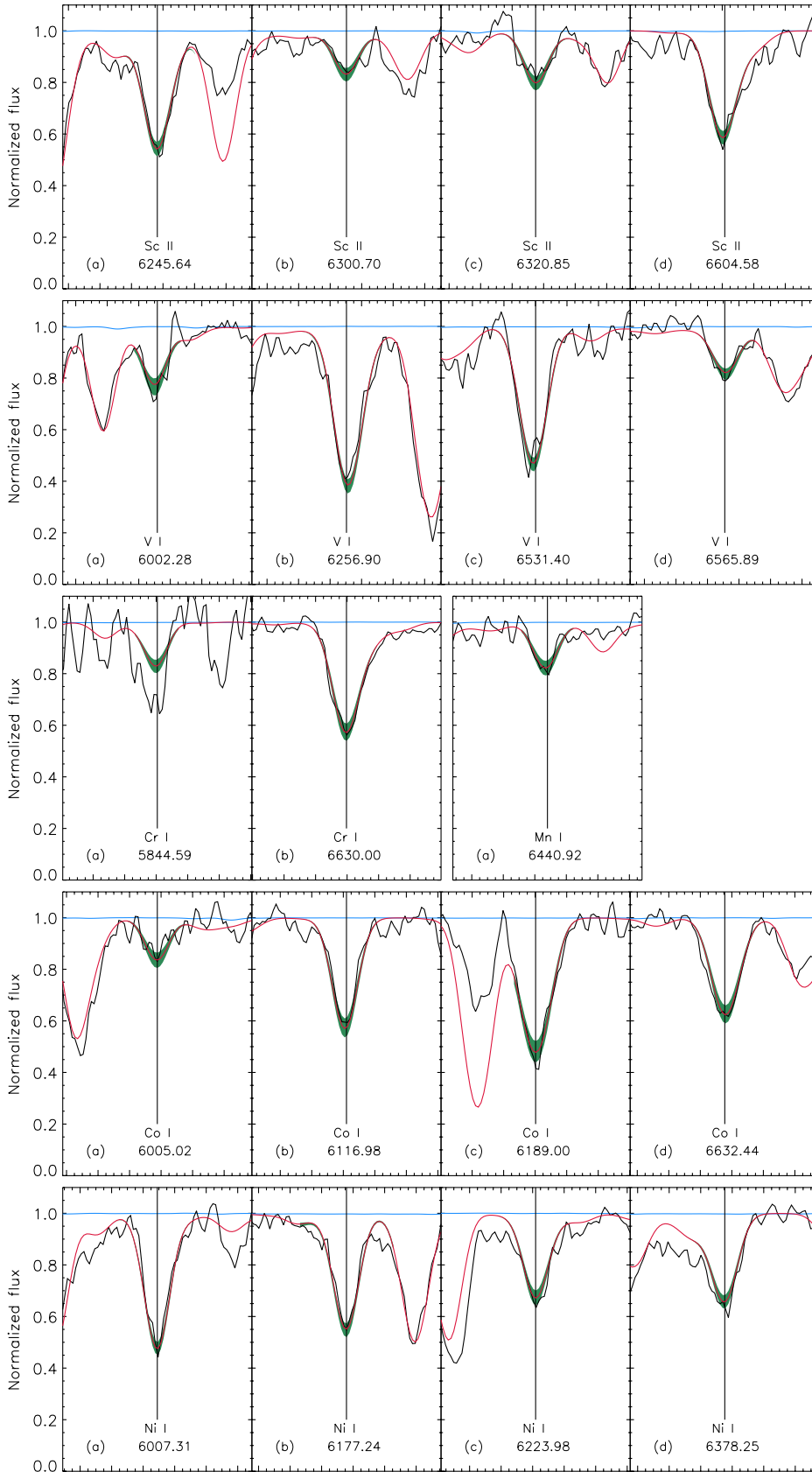


**Fig. B.4.** Stellar lines used for the calculations of the line-by-line abundance scatter and for the abundance determination in the analysis in the spectrum of B3-f1 (same color notations and axes as in Fig. B.3). The Cr I line in panel a is strongly affected by the noise and was not used in the final abundance measurement.